Chapter 6
The Quiet-Sun Corona

6.1 Solar Eclipses

Total solar eclipses provide a unique view of the faint solar corona, without the bright over-powering emission from the solar disk, enabling us to explore the electron density, temperature, thermodynamics, and related fundamental physics (Habbal et al. 2010a, 2011, 2013). In the past, solar eclipse observations were leading to fundamental tests of Einstein's theory of special relativity, by Sir Arthur Eddington in 1919, and to the discovery of coronal holes, by Max Waldmeier in 1957 (Bleeker et al. 2001).

The brightness of the white-light corona on 2008 August 1 and 2009 July 22, when solar activity was at its lowest in 100 years, was found to be $\approx 0.4 \times 10^{-6}$ of the total brightness of the Sun, which is the lowest ever observed (Hanaoka et al. 2012).

In a gravitationally stratified atmosphere, the electron density (or gas pressure) falls off exponentially with height, i.e., $n_e(h) \propto e^{-h/\lambda}$, where λ is the density scale height. EUV emission observed in ionized iron lines (such as Fe IX 171 Å or Fe XII 193 Å), has an intensity that is proportional to the squared density due to the collisional excitation mechanism. The emission in coronal forbidden lines, such as Fe X 6374 Å, Fe XI 7892 Å, Fe XIII 10,747 Å, and Fe XIV 5303 Å, is produced by collisional excitation (close to the Sun), and is dominated by resonant excitation when collisional excitation becomes too weak. Resonant absorption is proportional to the ion density, and the disk radiation at that wavelength. The different functional dependence of the emitted intensity in white-light and in EUV wavelengths has the consequence that EUV emission can only be observed in relatively low altitudes ($\lesssim 1.25 R_\odot$), while the white-light corona can be observed out to much larger distances from the Sun, which plays an important role during solar eclipses. In order to optimally enhance the fine structure of the corona in eclipse pictures, a *Fourier normalizing-radial-graded filter (FNRGF)* (Druckmüllerova et al. 2011), or an *Adaptive Circular Highpass Filter (ACHF)* is applied, see example in Fig. 6.1.

M. J. Aschwanden, *New Millennium Solar Physics*, Astrophysics and Space Science Library 458, https://doi.org/10.1007/978-3-030-13956-8_6

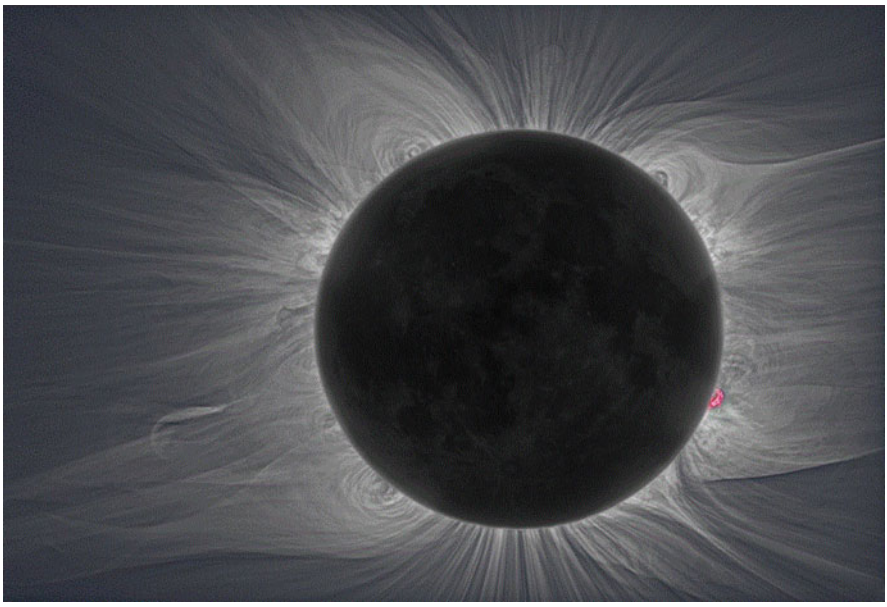

Fig. 6.1 White-light image of the corona taken by M. Druckmüller during the total solar eclipse of 2010 July 11. The image has been processed with the *Adaptive Circular Highpass Filter (ACHF)*, in order to enhance the fine structure (Habbal et al. 2011)

Electron density profiles $n_e(h)$ as a function of the radial distance from the Sun can be obtained from the white-light brightness by inversion of the line-of-sight integral, assuming Thomson scattering in the plane-of-sky. The density profile can be parameterized by a polynomial, e.g., $n_e(r) = \Sigma_k a_k r^{-k}, k = 1, \ldots n$ (Skomorovsky et al. 2012).

Temperature information in a solar eclipse picture can readily be obtained from the forbidden green and red line emission. The 4 eclipse pictures shown in Fig. 6.2 display the solar corona during the solar cycle minimum (2006) and near the solar cycle maximum (2010). There appears to be a bimodal distribution of temperature structures: Field lines extending outwards from the solar surface are dominated by cooler emission of Fe XI 7892 Å (peak $T = 1.1$ MK, red), while the bulges of streamers are dominated by the hottest emission of Fe XIV 5303 Å (peak $T = 1.8$ MK, green) (Habbal et al. 2013). Analysis of Fe XI 7892 Å images of the 2006 March 29 eclipse revealed localized increases in Fe XI density relative to the electron density, which is attributed to the dominance of radiative over collisional excitation in the formation of the Fe XI line (Habbal et al. 2007; Byhring et al. 2011). The 2006 and 2008 eclipses demonstrated that *prominence cavities* are intricate magnetic and density structures that are enshrouded with hot plasma (with a temperature of $\gtrsim 2.0$ MK) and twisted magnetic structures (Habbal et al. 2010b). Other diagnostic capabilities of forbidden lines are: (i) the inference of elemental abundances in the corona, which can be compared to their photospheric values,

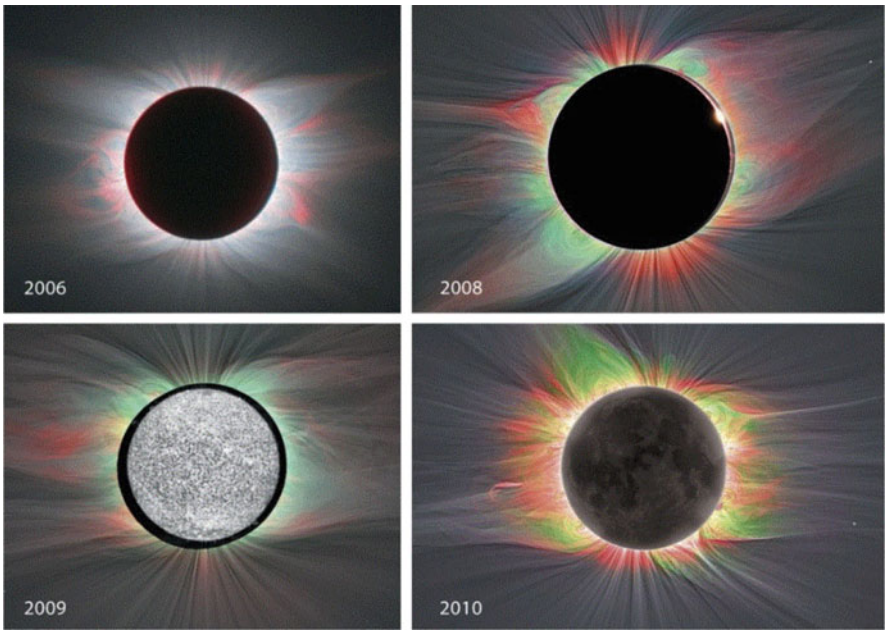

Fig. 6.2 Electron temperature distribution in the corona as inferred from narrow-band multi-wavelength observations form the eclipses of 2006, 2008, 2009, and 2010. Structures shown in grey are from the white-light images. Superimposed on this background is the emission from Fe XI 7892 Å ($T \approx 1.1$ MK; red), and Fe XIV 5303 Å ($T \approx 1.8$ MK; green), (Habbal et al. 2013)

(ii) the inference of the magnetic field direction and strength from polarization measurements, and (iii) the chemical composition of exogenic material from sun-grazing comets or near-solar asteroids (Habbal et al. 2013).

Coronal phenomena observed during eclipses include polar plumes, loop oscillations, quiescent or eruptive prominences (Alzate et al. 2017), tethered prominence-CME systems (Druckmüller et al. 2017), CMEs, erupting spicules and macrospicules, mass motion in the upper chromosphere, rays, streamers, the large-scale coronal magnetic field (Nandy et al. 2018), the center-to-limb variation of the solar brightness, the solar radius (Lamy et al. 2015), etc. Besides these widely-used phenomena, new morphologies of coronal structures in white-light eclipse images were discovered, such as *"smoke rings"*, *faint nested expanding loops, expanding bubbles*, and *twisted helical structures*, which are believed to be snapshots of the dynamical evolution of instabilities developing at prominence-corona interfaces, which propagate outward with the solar wind (Druckmüller et al. 2011). Unraveling of prominences and the outward expansion of the helical twisted field has been observed during eclipses also, which may point to the solar origin of interplanetary flux ropes (Habbal et al. 2014).

6.2 Quiet Sun: Flows and Jets

The more we improve the spatial and temporal resolution of solar observations, the more the term "Quiet Sun" becomes a misnomer. There are apparently ubiquitous Quiet-Sun phenomena that display transient flows and formation of jets, which involve "not-so-quiet", or even "violent" magneto-hydrodynamic processes. Nevertheless, the term is still useful to distinguish those parts of the corona that are not part of active regions (dominated by flare processes) or coronal holes (harboring the source regions of the fast solar wind). In the following we highlight recent observations of flow and jet phenomena in the Quiet Sun (Table 6.1).

Small-scale Hα upflow events were observed in the Quiet Sun with the BBSO, with typical sizes of $\approx$ 2.5″, blue-shifted velocities of $\approx$ 5 km s^{-1}, lifetimes of $\approx$ 1.4 min, and a birth rate of $\approx$ 78 events s^{-1} (Lee et al. 2000). They are different from dark mottles, which show both blue and red shifts (Lee et al. 2000).

Explosive events were observed with SUMER/SOHO in the Quiet Sun and exhibit bidirectional jets following a reconnection event, with high velocities of $\approx$ 100 km s^{-1}, spatial sizes of $\approx$ 2″ (1500 km), average lifetimes of $\approx$ 1 min, temperatures of 3×10^4–3×10^5 K, and a birth rate of $\approx$ 600 s^{-1} (Peter and Brkovic 2003). While the feature of bidirectional jets generally indicates magnetic reconnection, some explosive events were interpreted in terms of flux cancellation, or as a miniature CME with EUV dimming (Innes and Teriaca 2013).

Dynamic fibrils are thin jet-like extrusions that are formed in the vicinity of photospheric magnetic field concentrations, but extend out to the Quiet Sun and reach heights of 2000–10,000 km, and have durations of 3–10 min. Phenomena like dynamic fibrils, mottles, and spicules (Fig. 5.5) are all believed to be driven by magneto-acoustic shocks (Hansteen et al. 2006; De Pontieu et al. 2007a). Spicules

Table 6.1 A compilation of recent observations of Quiet-Sun transient phenomena, with interpretation of their drivers

Phenomenon	Interpretation	References
Hα upflow events	Magnetic reconnection	Lee et al. (2000)
Blinkers	Chromospheric heating	Peter and Brkovic (2003)
Dynamic fibrils	Magneto-acoustic shocks	Hansteen et al. (2006)
Spicules (limb) type-I	Magneto-acoustic shocks	De Pontieu et al. (2007a)
Spicules (limb) type-II	Magnetic reconnection	De Pontieu et al. (2007b)
Elongated dark mottles (disk)	Magneto-acoustic shocks	Rouppe van der Voort et al. (2007)
Reverse (soft X-ray) jet	Heat conduction or MHD wave	Shimojo et al. (2007)
Small-scale energy releases	Flux submergence	Potts et al. (2007)
High-speed upflows	Magnetic reconnection	McIntosh and De Pontieu (2009)
Miniature CMEs	Supergranular flows	Innes et al. (2009)
Explosive events	Magnetic reconnection	Innes and Teriaca (2013)
Jetlets in upper chromosphere	Fan-spine reconnection	Zeng et al. (2016)

are jet-like features at the limb, referred to as dynamic fibrils in active region plages, and as mottles in the Quiet Sun (Rouppe van der Voort et al. 2007).

Jetlets in the upper chromosphere can be triggered by magnetic fan-spine reconnection in emerging magnetic ephemeral regions (Filippov et al. 2007). The fan-spine geometry of the magnetic reconnection of a small-scale chromospheric jet event (Figs. 6.3 and 6.4) could be clearly resolved with the *New Solar Telescope (NST)* using 10,830 Å filtergrams (Zeng et al. 2016). Bi-directional flows were observed across the separatrix regions, suggesting that the jet was produced by magnetic reconnection in the upper chromosphere (Zeng et al. 2016). A jet propagating in a similar fan-spine geometry has been simulated by Wyper and DeVore (2016).

Reverse Soft X-ray Jets occur in the Quiet Sun at the secondary footpoint of a closed loop that produced a soft X-ray jet at the primary footpoint rooted in an active region. Such reverse jets have been observed with XRT/Hinode and are suspected to be produced by heat conduction, or by a MHD wave subsequent to the main jet (Shimojo et al. 2007).

Small-scale energy releases in the Quiet Sun can occur due to flux submergence, driven by the ubiquitous sub-photospheric convective downflows (Potts et al. 2007).

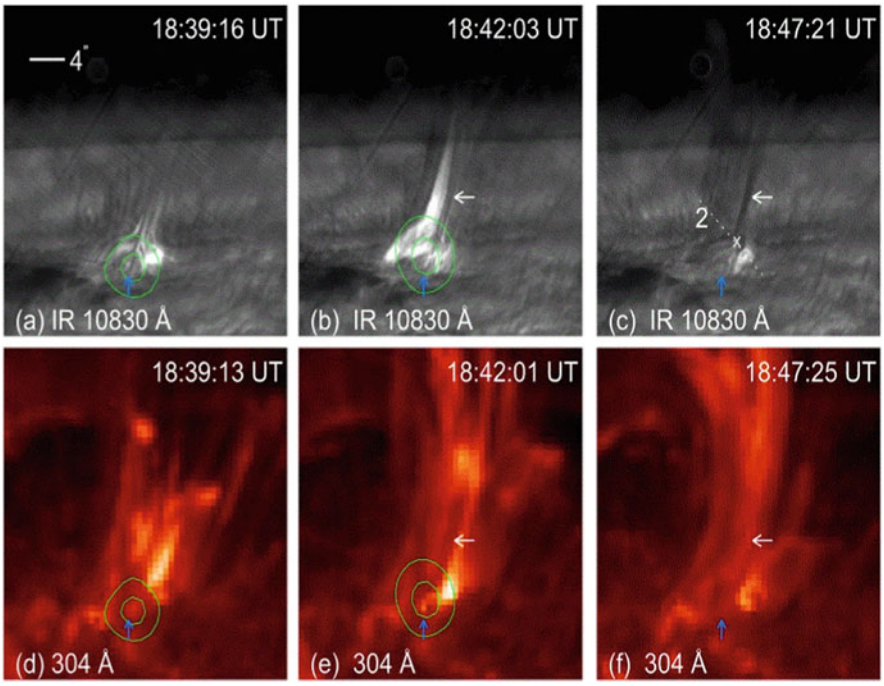

Fig. 6.3 Evolution of a jet event: 10,830 Å filtergrams (**a–c**), AIA 304 Å images (**d–f**). Green contours are RHESSI 6–12 keV emission, (Zeng et al. 2016)

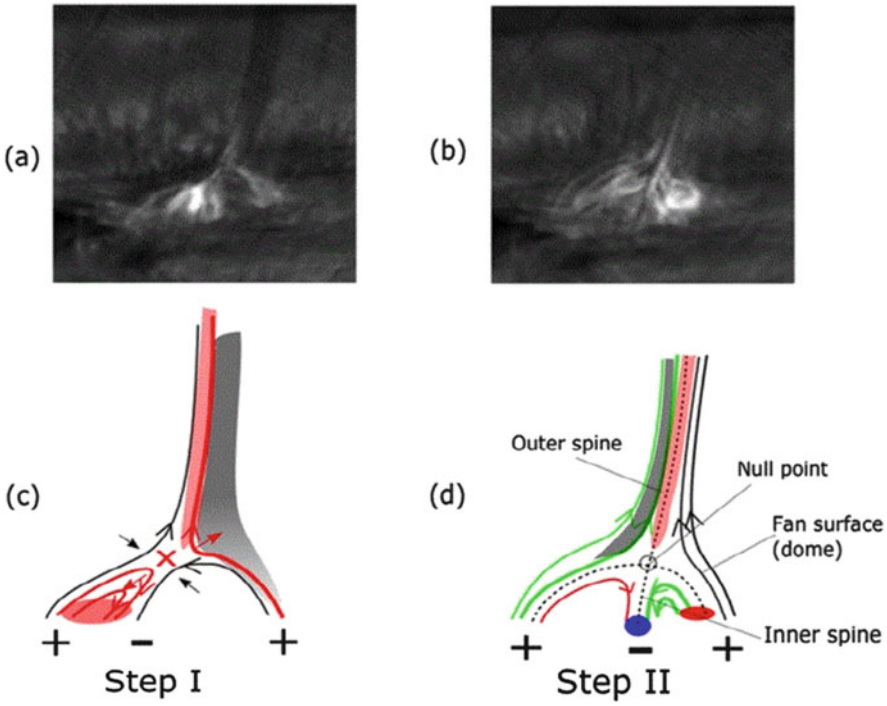

Fig. 6.4 Hα images (**a**,**b**) and diagram of fan-spine geometry of magnetic reconnection process (**c**,**d**), (Zeng et al. 2016)

Frequent high-speed (supersonic) mass downflows were inferred from SOT/Hinode measurements (Shimizu et al. 2008).

High-speed flows from the transition region into the corona in Quiet-Sun regions have been inferred from Si IV 1402 Å, C IV 1548 Å, N V 1238 Å, O VI 1031 Å, and Ne VIII 770 Å spectral lines observed with IRIS, which show a significant asymmetry in the blue wing of the emission line profiles. These high-speed upflows, preferentially occurring around the network regions, reveal upward velocities of order 40–100 km s^{-1} (McIntosh and De Pontieu 2009). This upflow component carries enough hot plasma to become significant for the energy and mass balance of the Quiet corona (McIntosh and De Pontieu 2009). These high-speed upflows are commensurable with speeds measured in type-II spicules (De Pontieu et al. 2007b). Plume-like structures, which generally carry high-speed outflows, are not only seen in coronal holes, but also in Quiet Sun regions (Tian et al. 2011). Ubiquitous Quiet-Sun jets have been detected also with IMAX/Sunrise and SOT/Hinode, based on the highly dynamic and strongly Doppler shifted Stokes V signals (Martinez Pillet et al. 2011), but no center-to-limb variation was detected (Rubio da Costa et al. 2015).

Miniature Coronal Mass Ejections (mini-CMEs) can be activated in the supergranular boundaries, where photospheric flows sweep up concentrations of

mixed polarity magnetic field. These mini-CMEs produce brightenings in EUV and faint waves with speeds of $\gtrsim 100$ km s^{-1}, with a rate of ≈ 1400 events per day on the whole Sun (Innes et al. 2009; Hong et al. 2011).

6.3 Quiet Sun: Cyclones and Tornadoes

Like the weather on Earth, cyclones, tornadoes, and hurricanes share the same property of rotational vortex motion. It is therefore no surprise that such vortical motions have been noticed in the solar corona recently (with SOHO and TRACE in late 1990s, and with SDO since 2010), mostly occurring in rotating prominences, but also in Quiet-Sun regions. Ancient reports of tornado-like prominences may go back as far as to Angelo Secchi in 1877.

While rotational motions on the Sun have been observed earlier, the discovery of *"cyclones"* rooted in *rotating network magnetic fields* was reported by Zhang and Liu (2011). The phenomenon of EUV cyclones is seen everywhere in the Quiet Sun, in all EUV channels of AIA/SDO (94, 131, 171, 193, 211, 304, 335 Å), and thus covers the full coronal temperature range of $T \approx 0.5$–2.5 MK. Observations and a *differential emission measure* analysis with EIS/Hinode suggest that there is more mass contribution in tornadoes at a temperature below $T = 1.0$ MK than in prominences (Levens et al. 2015). The rotational motion seen in EUV is also apparent in the line-of-sight magnetograms, and thus the rotating coronal plasma is tied to the rotation of the magnetic field, similar to the rotation of sunspots (Sect. 4.8). The rotation of cyclones has been tracked over several hours, but the lifetime of cyclones can last longer than 10 hours (Zhang and Liu 2011), up to 70–100 hrs in homologous cyclones (Xu et al. 2014). The rotation speed of cyclones was found in the range of $\approx 1°$–$5°$ per minute. After the cyclones rotate for several hours (Fig. 6.5), they can be followed by EUV brightenings (or microflares) and EUV waves. In a statistical survey of 388 *rotating network magnetic fields* near disk center, a mean unsigned magnetic flux of 4.0×10^{21} Mx (or 78% of the total network flux) was found, with the rotation showing a weak hemispheric preference (Zhang and Liu 2011). The rotation of the magnetic field about the vertical axis corresponds to an increase of the vertical current and helicity, as well as to an increase of the non-potential and free (magnetic) energy, and this way provides energy storage to be released in Quiet-Sun transients (see Sect. 6.2). Like magnetic tornadoes (Wedemeyer-Böhm et al. 2012), also other phenomena like cyclones may serve as energy channels into the solar corona, although this has still to be investigated. In a few cases, however, the causality may be reversed, i.e., flares may trigger a solar tornado (Panesar et al. 2013). The magnetic tornadoes appear to be driven by a combination of convective motion and conservation of angular momentum, while cyclones might be rather the result of a larger rotating magnetic field structure.

The likely explanation of the rotating motion of cyclones is the emergence of a helically twisted magnetic flux tube. In an observation by SOT/Hinode, such an emerging twisted flux tube, reminiscent of a cyclone, was found to produce

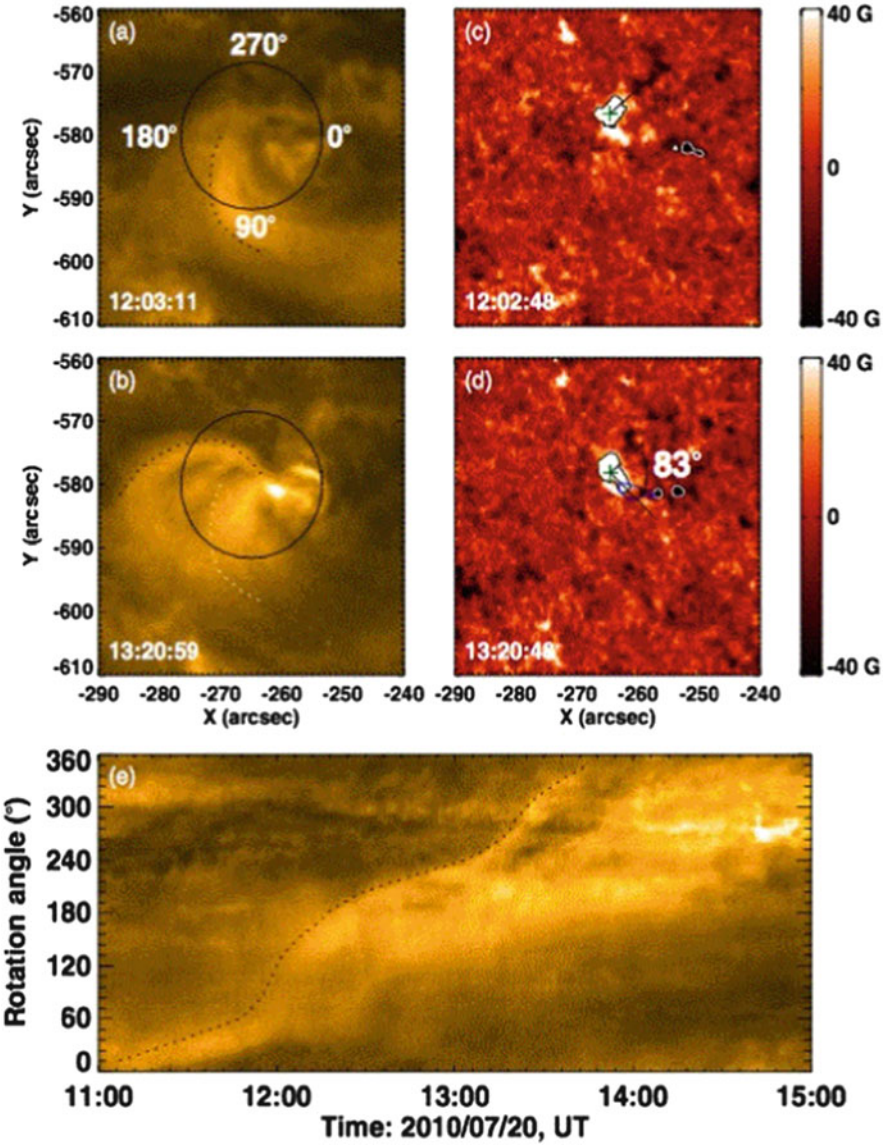

Fig. 6.5 AIA/SDO 171 Å images (**a**,**b**), HMI/SDO magnetograms (**c**,**d**), and a time-slice diagram of the rotation angle of a cyclone observed on 2010 July 20. (**e**) The rotation angle is 83° between the two times 12:03:11 UT and 13:20:59 UT (Zhang and Liu 2011)

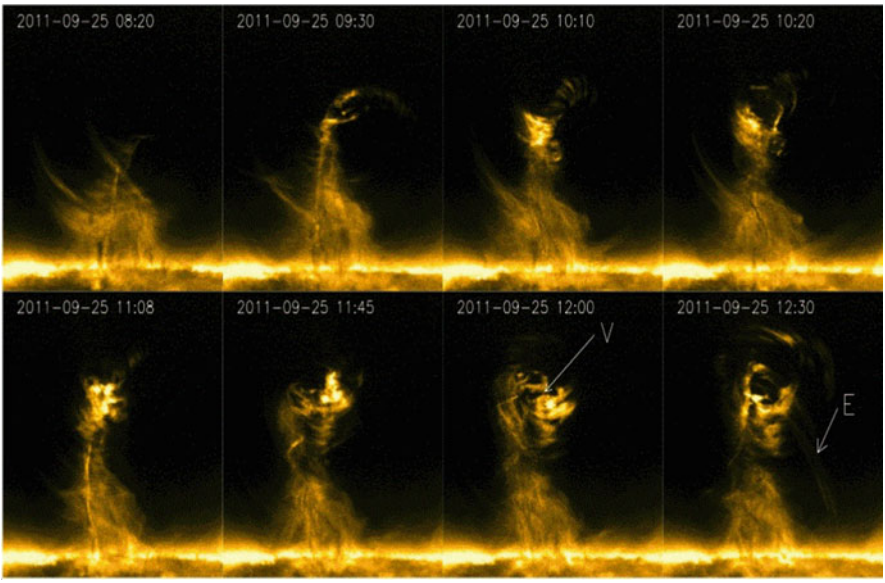

Fig. 6.6 Time evolution and rotation of a solar tornado seen in the AIA (171 Å) channel over ≈4 hrs, starting on 2011 September 25, 08:20 UT, at 8 different times (Li et al. 2012)

a chromospheric running wave, which could be reproduced with a 3-D MHD simulation (Magara et al. 2012).

Another type of solar tornadoes is the rotational flow and evolution of magnetic helicity in a *prominence cavity*. Such a configuration with a prominence seen at the limb and associated cavity, observed with AIA/SDO, has been reported by Li et al. (2012). The evolution during 3 hours shows material upflowing from the prominence core along a loop-like structure, accompanied by a rise ($\geq 50,000$ km) of the prominence core and the loop, producing small blobs and streaks of varying brightness rotating around the top part of the prominence and cavity (Fig. 6.6), mimicking a cyclone (Li et al. 2012). The cyclonic appearance is interpreted in terms of the expansion of helical structures into the cavity, and the movement of plasma along helical structures, which appears as a rotation when viewed along the helix axis (Li et al. 2012).

The relationship of so-called *solar magnetic tornadoes* with filaments or prominences became clearer when the rotational motion was disentangled above the limb, both in emission (He II 304 Å, Hα 6562.8 Å, Ca II K3 3934 Å, using AIA, NSO-GONG, and Meudon data), as well as in absorption (AIA, Fe IX 171 Å) (Su et al. 2012, 2014). A statistical study of 201 *giant tornadoes* yields an occurrence rate of 30 events to be present across the whole Sun, at a time near the solar maximum (Wedemeyer et al. 2013). The rotation of the tornadoes may progressively twist the magnetic field structure of a prominence until it becomes unstable and erupts (Wedemeyer et al. 2013). Recent studies focus on the helical kink instability of

prominences, which may be encountered in a tornado-like evolution (Wang et al. 2017).

As an alternative explanation, Panasenco et al. (2014) confronts us with the view that the tornado-like appearance of helically twisted prominences is mainly an illusion due to projection effects. Two different cases are discussed. One case of apparent vortical motion in prominence spines and barbs arises from the (mostly) 2-D counterstreaming plasma motion along the prominence spine and barbs, together with oscillations along individual threads. The other case of apparent rotational motion is observed in a prominence cavity and results from the 3-D plasma motion along the writhed magnetic fields inside and along the prominence cavity as seen projected on the limb. Thus, the "tornado" impression results either from counterstreaming and oscillations, or from the projection on the plane-of-the-sky of plasma along magnetic field lines, rather than from a true vortical motion around an (apparent) vertical or horizontal axis (Panasenco et al. 2014). Later spectroscopic work showed persistent blue and red Doppler shifts on the two opposite sides of the tornado (Su et al. 2014; Mghebrishvili et al. 2015; Schmieder et al. 2017; Yang et al. 2018), evidencing rotational motion of the tornado and weakening the *"vortical illusion"* argument of Panasenco et al. 2014). On the other side, tornado-like magnetic structures are only able to support prominences if sufficient twist or poloidal flows are present (Luna et al. 2015).

In contrast to cyclonic and tornado events in the Quiet-Sun corona, vortex motions have also been observed in the chromosphere. Observations with CRISP in the Ca II 8542 Å spectral line revealed *small-scale swirl events*, originally called *chromospheric swirls*, which typically consist of ring or ring fragments with widths of $\approx 0.2''$, diameters of $\approx 2''$, and Doppler shifts of -2 to -7 km s^{-1} (Wedemeyer-Böhm and Rouppe van der Voort 2009; Wedemeyer-Böhm et al. 2012). Numerical simulations show that the swirling motion, which occurs as photospheric vortex flows in the MHD simulations, indeed produces the spiral particle trajectories in the chromosphere (Wedemeyer and Steiner 2014).

6.4 Quiet Sun: Magnetic Field

The global magnetic field of the Sun can be modeled as a poloidal dipole during the solar minimum, turning into a toroidal field during the solar cycle maximum, according to the Babcock-Leighton dynamo model. In addition, strong local magnetic fields are produced by emerging flux in sunspots and active regions, which need to be superimposed onto the global field. The global magnetic field can then be further subdivided into zones of open magnetic fields (containing polar and trans-equatorial holes) and closed-field regions (the so-called Quiet Sun regions). In addition, there are ubiquitous and randomly distributed small-scale fields, called *salt-and-pepper* structure. Contrary to the general definition of coronal holes in terms of open field regions, closed loops were found to exist in coronal holes also, but their average length and height is lower than in the Quiet Sun (Wiegelmann and

Solanki 2004), essentially produced by the salt-and-pepper structure. We have to keep this compartmentalization in mind when we talk about the *Quiet-Sun magnetic field*.

The salt-and-pepper structure of positive and negative small-scale magnetic polarities appears to be randomly distributed on the photospheric solar surface, but a more careful examination of magnetograms reveals a hierarchy of network structures, mesogranular, supergranular, and giant cell structures, which all organize the inhomogeneous Quiet Sun magnetic field. The photospheric salt-and-pepper structure has also been called *"magnetic carpet"* and evolved into the *tectonic coronal heating model* (Priest et al. 2002), in analogy to geological tectonic plates that produce earthquakes (stressed energy releases) at their (network) boundaries (Fig. 6.7). The magnetic flux in the Quiet Sun is not static, but rather highly dynamic, as it emerges in ephemeral regions and quickly migrates to supergranule

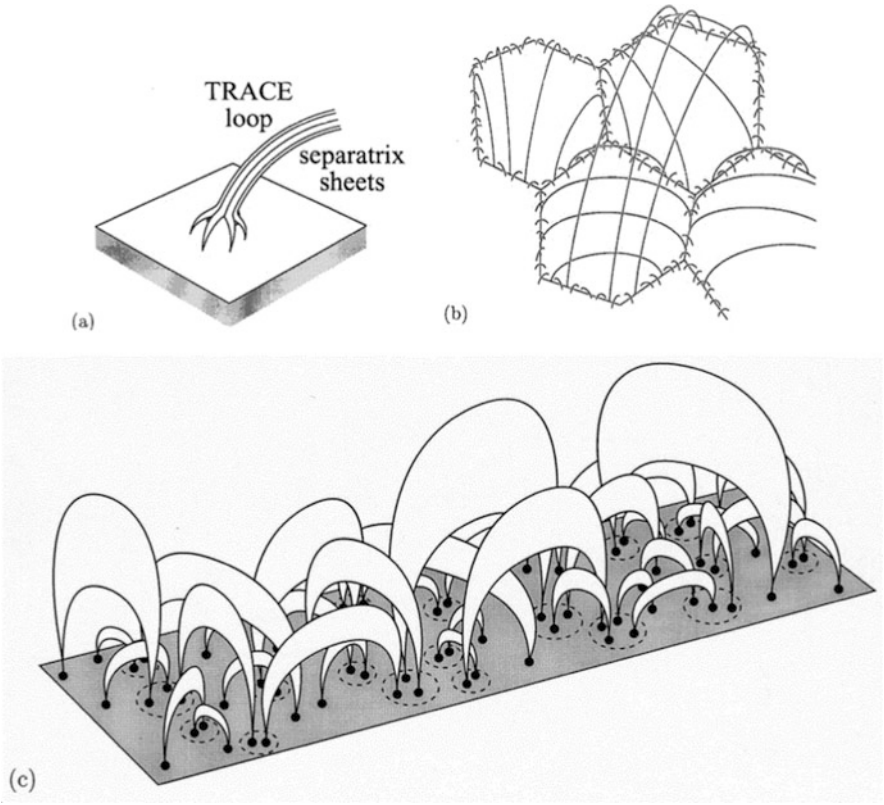

Fig. 6.7 (**a**) Coronal loop observed with TRACE, with a footpoint that ends as a spider of fingers separated by separatrix current sheets. (**b**) Over several supergranules a range of coronal loops (viewed from above) shows a mixture of short and long loops. (**c**) A 3-D view within the network indicates that the photospheric flux elements (dashed ovals) are in general connected to a range of neighbors (Priest et al. 2002)

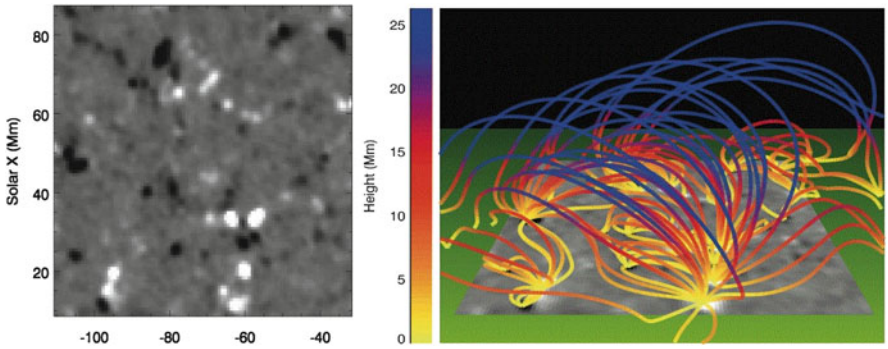

Fig. 6.8 *Left:* Magnetogram (80 × 80 pixels) showing the line-of-sight component of the photosphere, white is positive and black is negative magnetic polarity. *Right:* Magnetic field extrapolation based on the boundary condition of the observed magnetogram in left panel. The color indicates the height (from 0 to 25 Mm). Note that all field lines indicate a closed-field configuration, without open field lines (Close et al. 2004)

boundaries, merges, and cancels over time periods of 10–40 hrs. Most ($\approx$ 95%) of the photospheric flux closes low down in the chromosphere (Fig. 6.8), while only a small fraction ($\approx$ 5%) forms large-scale connections with the overlying corona. The time scale for magnetic flux connected to the Quiet-Sun corona is only $\approx$ 1.4 hr (Close et al. 2004), about 10% of the photospheric flux recycling time (Hagenaar 2001).

The measured magnetic field strength of the salt-and-pepper component depends very much on the spatial resolution of the instrument. Spectro-polarimetric measurements (Fe 6300 Å) of high-resolution data from Hinode (with 0.32″ resolution) indicate that the inter-network consists of very inclined $\approx$ 100 G fields, while the network exhibits a predominance of kG field concentrations (Orozco Suarez et al. 2007). The ubiquitous horizontal polarization on the edges of bright granules seen by Hinode are found to be invariant during a solar cycle, which lends support for a local dynamo (Buehler et al. 2013).

Modeling the Quiet Sun magnetic field by positioning flux concentrations on the edges of cells formed by Voronoi tesselation (to mimic the salt-and-pepper field) and applying observed loop scaling laws, it is found that the solar corona has a plasma-β close to unity, the corona exhibits dynamic fine structure, but no significant spatially averaged Doppler shift, which implies that the Quiet Sun corona is often neither quasi-steady nor force free, and thus MHD models are needed to model the coronal magnetic field (Schrijver and van Ballegooijen 2005).

The complexity of the solar magnetic field has been approached with topological methods (for a review see Longcope 2005), which characterizes the field by separators, separatrices, quasi-separatrix layers, null points, fans, spines, skeletons, and bald patches (related to "saddle points" in mathematical terminology). Topological models, such as the *magnetic charge topology model*, the *pointwise mapping model*, or the *submerged pole model* help to compartmentalize the magnetic

field into unipolar magnetic regions, to quantify magnetic connectivities between different polarities, and to understand the connectivity changes during a magnetic reconnection process. A relationship between the number of domains (D), number of magnetic unipolar sources (S), the number of separators (X), and the number of coronal nulls (N) is,

$$D = S + X - N - 1 \,. \tag{6.4.1}$$

The salt-and-pepper structure of the magnetic field in the Quiet Sun produces many *magnetic separators*, since many separators arise from each null point (Close et al. 2005). Based on a study with SOT/Hinode, null points are found mostly to be located above the bottom boundary layer in the photosphere (54%) and in the chromosphere (44%), with only a few null points in the corona (2%), which emphasizes the topological complexity in the chromosphere, while the corona exhibits a simpler field geometry, and coronal heating involving an X-point in a magnetic reconnection process is less likely than in the chromosphere (Régnier et al. 2008; Longcope and Parnell 2009). This is also consistent with modeling magnetic loops in the Quiet Sun using IMAX/Sunrise data, from which it is found that 91% of the magnetic energy in the mid-chromosphere (at a height of 1000 km) is in a field line whose stronger footpoint has a strength of more than 300 G, which is above the equipartition field strength with convection (Wiegelmann et al. 2010).

Dynamical models of the global solar magnetic field include differential rotation, supergranular diffusion, meridional flows, magnetic flux emergence (for a review see Mackay and Yeates 2012). The major requirement of global models is the interpolation of magnetograms to the back-side of the Sun, which became known as *synoptic magnetograms*. For the computation of such global coronal magnetic field models, a number of methods have been invented, such as the *Potential Field Source Surface (PFSS)* model, *Nonlinear Force-Free Field (NLFFF)* models, or *magneto-hydrostatic (MHS)* models (for a review see Wiegelmann et al. 2014, 2017). Comparisons between the extrapolation methods exemplify the dependence on the computational domain (Tadesse et al. 2015), and on the spatial resolution (DeRosa et al. 2015). Significant improvements of the computed NLFFF solutions can be obtained by fitting automatically detected loops and fibrils with the *Vertical Current Approximation (VCA-NLFFF)* code (Aschwanden et al. 2016). Another improvement of NLFFF codes involves "inductive" electric field solutions obtained from a surface flux-transport model (Weinzierl et al. 2016). A novel method involves the kinematics of *"EIT waves"* during their global propagation over the solar surface to calculate the magnetic field (Long et al. 2013).

6.5 Quiet Sun: Photosphere-Corona Connectivity

There is an intimate coupling between the photosphere and the corona, as exhibited by close correlations between the photospheric magnetic field strength B and the soft X-ray luminosity L_{SXR} of the corona. While some correlation $B \propto L_{SXR}$ is

expected in active regions (Benevolenskaya et al. 2002), where soft X-ray emission is produced by magnetic reconnection processes and subsequent plasma heating during flares, it is perhaps surprising to find a coupling in Quiet-Sun regions (Pevtsov and Acton 2011), even far away from flaring active regions.

A study on the soft X-ray luminosity and photospheric magnetic field was undertaken with SXT/Yohkoh and KPNO magnetograms during almost a full solar cycle (1991–1998), in 3 selected field-of-views at the central meridian (Pevtsov and Acton 2011). The soft X-ray luminosity decreased by a factor of 7 between 1991 (active Sun) and 1996 (quiescent Sun), while the unsigned magnetic flux decreased only by a factor of 2. The soft X-ray luminosity exhibited also variations on time scales of 9–12 months, which were not present in the magnetic flux, which implies that the Quiet-Sun magnetic elements (*chromospheric network, "magnetic carpet", or "salt-and-pepper fields"*) can at best account for a minimal contribution to the heating of the 1–2 MK corona, while the major contribution to coronal heating has to be associated with the stronger magnetic fields in active regions (Pevtsov and Acton 2011).

Another correlation study between the photospheric magnetic field and the EUV brightness of the coronal plasma was conducted by using MDI/SOHO magnetograms and EIT/SOHO Fe XII (195 Å) images for a total duration of 4 days (Handy and Schrijver 2001). The findings are that emerging bipoles in the Quiet Sun reach a typical length of $\approx$ 14 Mm before fading or reconnecting in a time period of $\approx$ 5–12 hrs, and the Quiet Sun decorrelates in $\approx$ 15 hrs. The majority of coronal loops in the Quiet Sun were found to be products of numerous small-scale magnetic flux concentrations coalescing in the photosphere, rather than being produced by a single large emerging bipole (Handy and Schrijver 2001).

A recent study explores the statistics and occurrence probability distributions of coronal EUV brightening events (observed with EUVI/STEREO) and the photospheric counterparts (detected in magnetograms from MDI/SOHO), sampled over a time duration of one month (Uritsky et al. 2013). Interestingly, the majority of coronal dissipation sites do not show an obvious correlation with the underlying photospheric field. However, both distributions are power law-like, suggesting that the multi-scale intermittent dissipation in the corona at spatial scales $>$ 3 Mm is controlled by turbulent photospheric convection. The complex topology of the photospheric network makes this coupling essentially nonlocal and non-deterministic. The lack of detailed correlations has been predicted by Schrijver and Title (2002), which is described as *stochastic coupling* of the solar photosphere with the corona (Uritsky et al. 2013). This is a fundamental property of nonlinear energy dissipation systems, in the sense that a random disturbance (in the photosphere) can be nonlinearly amplified to a small or large avalanche event (in the corona), a property that is also called *self-organized criticality*. Although both input (disturbances) and output (avalanche) events have similar (power law-like) occurrence (size) distribution, the size of an individual avalanche event cannot be predicted from the size of the triggering disturbance.

Magnetic field computations in the Quiet Sun are challenging because of the complex topology at the spatial resolution limit of current instrumentation. The topological domains of mixed-polarity magnetic potential fields have been analyzed

from TRACE and MDI/SOHO data, leading to the conclusions that (i) we should expect at best a weak correlation between coronal brightness and the magnetic flux in the underlying flux concentrations, (ii) that low-lying chromospheric field lines can be traced in Hα fibrils to obtain complementary information to traced EUV loops in coronal heights, and (iii) that Parker's prediction of footpoint braiding is more efficient low in the corona (rather than in the high corona) and in Quiet-Sun regions (rather than in active regions) (Schrijver and Title 2002). Magnetic field modeling of IMAX/Sunrise data exhibited a rapid connection recycling time of $\approx 3 \pm 1$ min in the upper atmosphere and $\approx 12 \pm 4$ min in the photosphere (Wiegelmann et al. 2013).

The magnetic connection between the solar photosphere and the corona has often been characterized with a wineglass-shaped magnetic canopy of network flux that fully encloses weakly magnetic regions below it (Fig. 6.9 left), which was

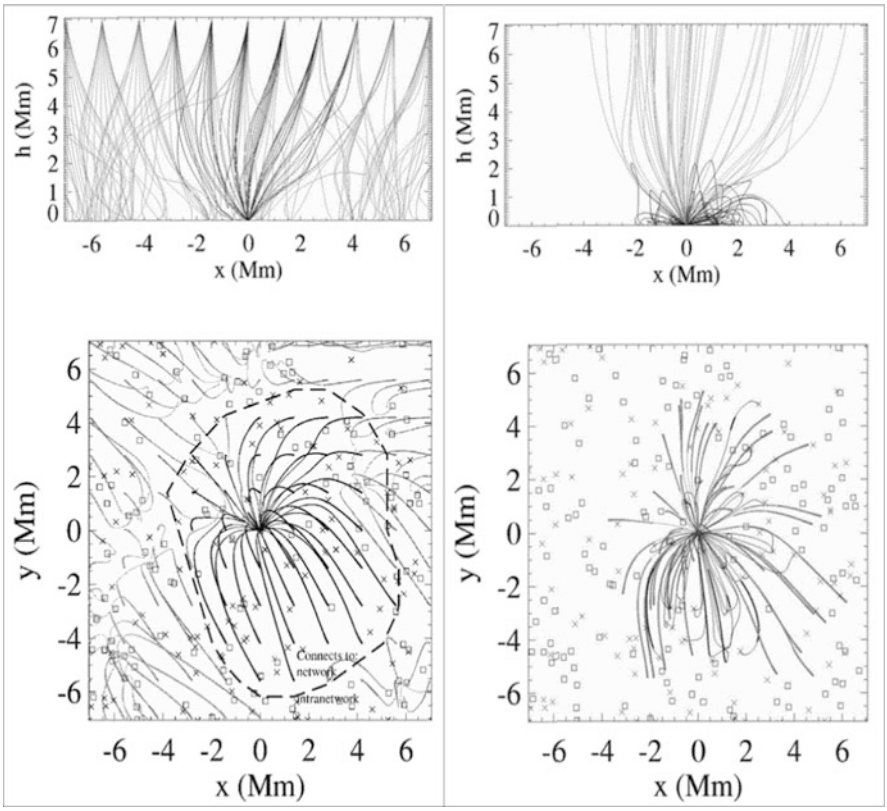

Fig. 6.9 *Left:* Magnetic field extrapolation from a regular grid at an altitude of $h = 7$ Mm, which illustrates the classical network canopy that covers the entire photosphere. *Right:* Magnetic field extrapolation from network concentrations with a flux of 3×10^{18} Mx in very Quiet-Sun regions, surrounded by a small-scale mixed polarity field (Schrijver and Title 2003)

later considered as fundamentally wrong (Schrijver and Title 2003). Instead, in the presence of a relatively strong internetwork field, as much as half of the coronal field over very Quiet Sun may be rooted in the mixed-polarity internetwork field throughout the supergranules (Fig. 6.9 right), rather than in the previously assumed network flux concentrations (Schrijver and Title 2003; Wedemeyer-Böhm et al. 2009). Even more pessimistic, magnetic field models with kG internetwork flux elements demonstrated that one cannot really determine with current instrumentation from observations, which regions on the Quiet-Sun surface, i.e., the network or internetwork, are connected to which parts of the corona through extrapolation techniques (Jendersie and Peter 2006).

Theoretical scenarios of the photosphere-corona coupling in the Quiet Sun involve post-reconnection shocks and sling-shot effects in the photosphere and chromosphere (Ryutova et al. 2001), the tectonic coronal heating model (Priest et al. 2002), magnetic reconnection in quasi-separatrix layers and hyperbolic flux tubes (Titov et al. 2002), generalized squashing factors for a covariant description of magnetic connectivity (Titov 2007), and 3-D MHD simulations of subphotospheric magneto-convection (e.g., Abbett 2007).

A summary diagram of the complex concepts of the photosphere-corona coupling is shown in Fig. 6.10, which includes phenomena such as granulation, supergranulation, photospheric network, p-modes, g-waves, small-scale canopies, weak fields, current sheets, shock waves, fibrils, dynamics fibrils, type-I and type-II spicules, Alfvén waves, etc. (Wedemeyer-Böhm et al. 2009; Lagg et al. 2017). The solar magnetism is a multi-scale system in which low-flux magnetism plays a crucial role, coupling different layers of the atmosphere (Martinez-Gonzalez et al. 2010).

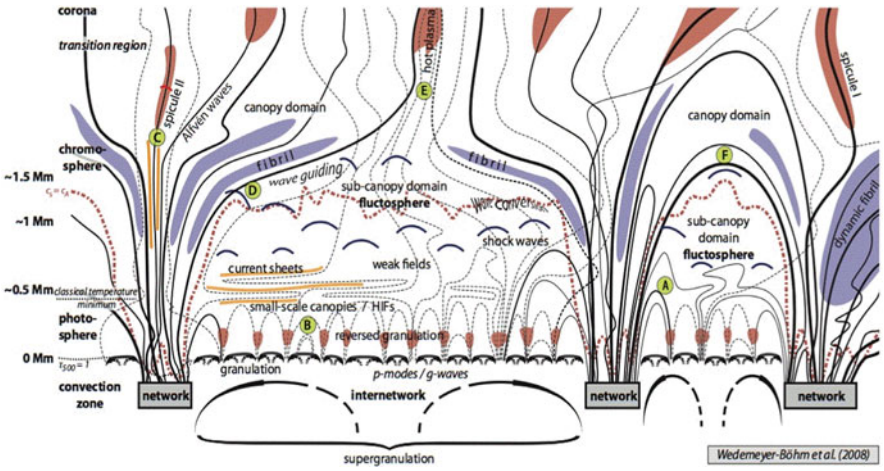

Fig. 6.10 Schematic diagram of the coupling between the convection zone, the photosphere, chromosphere, transition region, and corona (Wedemeyer-Böhm et al. 2009)

6.6 Quiet Sun: Alfvénic Waves

Theoretical studies concluded that dissipation of Alfvén waves is not an effective heating mechanism for the transition region and corona, although it may be for the chromosphere (e.g., Campos and Mendes 2000). In a partially ionized chromosphere, the dominant damping process of Alfvén waves is due to collisions between ions and neutrals (De Pontieu et al. 2001; Khodachenko et al. 2004; Leake et al. 2005; Song and Vasyliunas 2011; Tu and Song 2013). For a given wave frequency, the maximum damping always occurs at temperature minimum heights and in the coldest structures. Alfvén waves with frequencies above 0.6 Hz (or $\lesssim 1.7$ s) were found to be completely damped, and frequencies below 0.01 Hz (or $\gtrsim 100$ s) unaffected (Leake et al. 2005). The chromosphere behaves like a low-pass filter and the magnetic field strength determines the upper cutoff frequency. For coronal loops, the presence of a moderate amount of Alfvén wave damping in the chromosphere can enhance wave leakage at the loop footpoints (De Pontieu et al. 2001), which is a likely mechanism for damping of coronal loop oscillations, as first observed in TRACE data.

Early numerical simulations of small-scale flux tubes (with diameters of 100 km) in the granular network of the Quiet Sun have been studied in terms of strong currents conveyed by nonlinear torsional and compressional waves, and it was found that Alfvénic wave energies can be transferred upward in both untwisted and highly twisted flux tubes and eventually contribute to coronal heating (Sakai et al. 2001). Another simulation on dissipated Alfvén waves in an inhomogeneous 3-D force-free equilibrium model above a Quiet Sun region exhibited partial reflection of waves and demonstrated that a non-negligible fraction of the Alfvén wave energy is dissipated inside the corona (Malara et al. 2005), taking place mainly in magnetic separatrices (Malara et al. 2007).

The search for waves in the Quiet Sun corona started around the new millennium, with space-borne instruments (SOHO/EIT, Yohkoh), as well as with ground-based coronagraphs, e.g., in green-line (Fe XIV 5305 Å) spectra with the *Norikura Solar Observatory*, from which Alfvénic wave speeds of ≈ 500 km s^{-1} and sound waves with wave speeds of ≈ 100 km s^{-1} were reported (Sakurai et al. 2002). The line intensity and line width (of sound waves) did not show clear oscillations, but their phase relationship with the Doppler velocity $(\delta I/I) = 2(v/c_s)$ (with sound speed $c_s \propto \sqrt{T}$) indicated propagating waves rather than standing waves.

A breakthrough in the detection of Alfvén waves in the solar corona was accomplished with the *Coronal Multi-Channel Polarimeter (CoMP)* instrument at the *National Solar Observatory (NSO)* New Mexico, by using the Fe XIII 10,747 Å coronal emission line, which provided intensity, line-of-sight velocity, and linear polarization images (Tomczyk et al. 2007). Ubiquitous upward propagating waves were seen (Fig. 6.11), with phase speeds of 1000–4000 km s^{-1}, and trajectories consistent with the direction of the magnetic field inferred from the linear polarization measurements. The type of MHD waves that was most consistent with the observations was believed to be Alfvén waves, because the observed phase

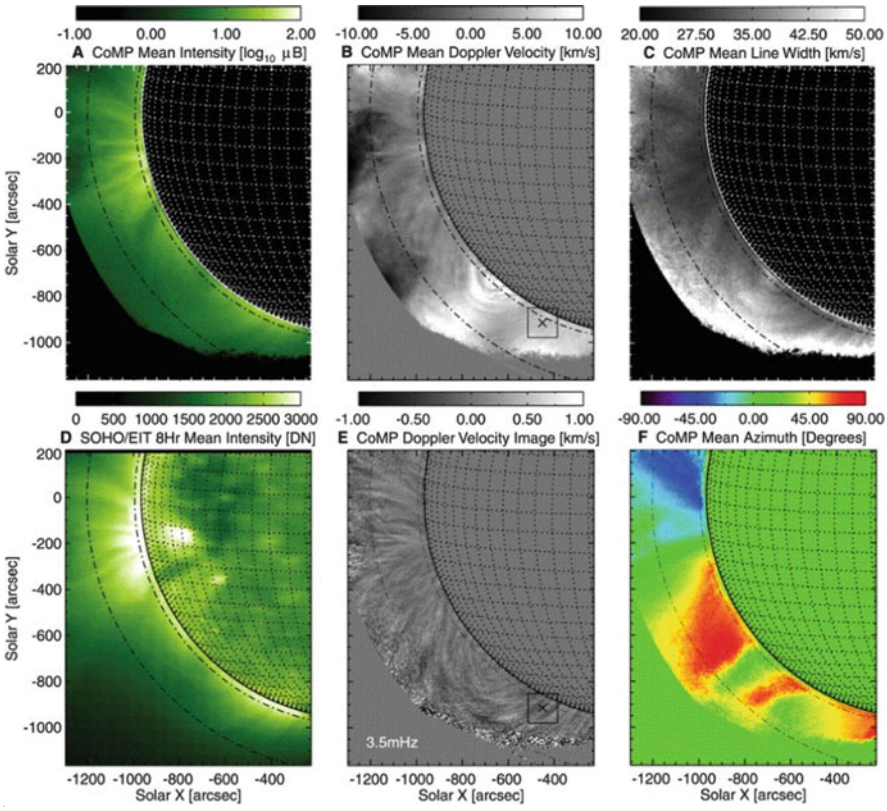

Fig. 6.11 (**a**) CoMP mean intensity [$\log_{10} \mu B$]; (**b**) CoMP mean Doppler velocity [km s^{-1}]; (**c**) CoMP mean line width [km s^{-1}]; (**d**) SOHO/EIT 8 hr mean intensity [DN]; (**e**) CoMP Doppler velocity image [km s^{-1}]; (**f**) CoMP mean azimuth [degrees] (Tomczyk et al. 2007)

speeds (1000–4000 km s^{-1}) are much larger than the sound speed ($\approx$ 200 km s^{-1}) and therefore the waves are not slow magneto-acoustic mode waves. The spatio-temporal properties of the velocity oscillations and the linear polarization measurements show that these waves propagate along the fields, which would not be the case for fast magneto-acoustic waves. The power of these detected Alfvén waves, however, was found to be insufficient to heat the corona.

While the previous detection of Alfvénic waves in the corona (Tomczyk et al. 2007) revealed oscillation amplitudes far too small (0.5 km s^{-1}) to supply the energy flux of (1–2) $\times$ 10^5 erg cm^{-2} s^{-1}, which is required to drive the fast solar wind or to balance the radiative losses of the Quiet Sun corona, new measurements were presented, using He II 304 Å and Fe IX 171 Å data from AIA/SDO, where transverse swaying motion of coronal loops (Fig. 6.12) were interpreted as the response to passing Alfvénic waves through plasma at $\approx$ 10^5 K (in the transition region) or at coronal temperatures (McIntosh et al. 2011). The ubiquitously observed

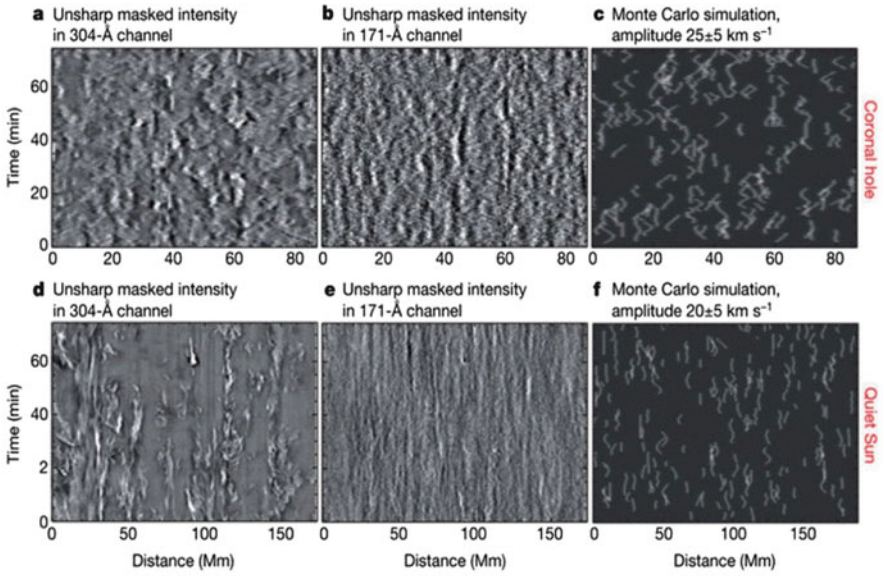

Fig. 6.12 Examining Alfvénic motion in coronal hole (top row) and Quiet Sun (bottom row) regions. (**a**–**e**) AIA/SDO space-time plots of unsharp masked intensity in the 304 Å (**a**,**d**) and 171 Å (**b**,**e**) channels 15 Mm above the solar limb. (**c**,**f**) Monte-Carlo simulations for Alfvénic waves with periods of 150–600 s and amplitudes of 25 ± 5 (**c**) and 20 ± 5 km s^{-1} (**f**). These simple simulations indicate that the spatio-temporal superposition of many independent bright features carrying Alfvénic waves with random phases leads to poor visibility of the extrema of the sinusoidal motion. The polarization of the Alfvénic wave is along the line-of-sight (McIntosh et al. 2011)

outward-propagating Alfvénic motions have periods of the order of 100–500 s throughout the quiescent atmosphere, and thus carry sufficient energy to heat the Quiet corona (McIntosh et al. 2011). Furthermore, compressible (sound waves) and incompressible wave modes (Alfvénic waves) have both been identified in on-disk observations also, which indicates a vast reservoir of wave energy in the chromosphere (Morton et al. 2012).

Analysis of CRISP/SST Hα 6562.8 Å observations revealed the ubiquitous presence of high-frequency ($\approx$ 12–42 mHz, or 20–80 s) torsional motions in thin spicular-type structures in the chromosphere of the Quiet Sun, which by means of numerical simulations were identified as *torsional Alfvén waves* (Srivastava et al. 2017). The associated high-frequency drivers in the chromosphere were estimated to contain a huge Poynting flux of $\approx 10^8$ erg cm^{-2} s^{-1}, while less than $\lesssim 1\%$ transmission to the corona would be sufficient to heat the corona and to energize the (supersonic) solar wind (Srivastava et al. 2017).

6.7 Quiet Sun: Heating Mechanisms

The *coronal heating problem* is one of the most prominent unsolved mysteries in solar physics. Bluntly stated: Why does the coronal temperature increase from $\approx$ 5800 K on the photospheric surface to several million degrees in the corona? A differentiation in the answer must be made for at least three different magnetic regimes in the solar corona: (i) active regions (with closed magnetic fields), (ii) the Quiet Sun region (with closed magnetic fields), and (iii) coronal holes (with open magnetic fields). The energy balance is somewhat different for open-field configurations, where the plasma can flow away, and for closed-field structures, where an equilibrium can be reached. The heating rates or Poynting fluxes required to balance conductive and radiative losses are therefore different in the three regimes, i.e., $E \approx 8 \times 10^5$ erg cm^{-2} s^{-1} ($T_e \approx 0.8$ MK) for coronal holes, $E \approx 3 \times 10^5$ erg cm^{-2} s^{-1} ($T_e \approx 1.5$ MK) for the Quiet Sun, and $E \approx 10^7$ erg cm^{-2} s^{-1} ($T_e \approx 2.5$ MK) for active regions, which is also reflected in the different (mean) temperatures. Most of the proposed physical heating mechanisms can be classified into two major categories, AC (alternating current) models such as faciliated by high-frequency waves, and DC (direct current) models such as generated by twisting and braiding of coronal loops. There has been significant progress and evidence for both types of models since the new millennium, so that the question has to be refined to the relative contributions of AC versus DC currents. Recent reviews on the coronal heating problem can be found in DeMoortel and Browning (2015) and Klimchuk (2015).

AC wave heating models experienced a strong boost after the detection of Alfvénic waves with SOT/Hinode, which detected Alfvén waves in chromospheric spicules with strong amplitudes of the order of 10–25 km s^{-1} and periods of 100–500 s. The energy flux in the chromosphere was estimated to be $E = \rho v^2 v_A \approx$ (4–7) $\times 10^6$ erg s^{-1} cm^{-2}, based on the Alfvén speed $v_A = B/\sqrt{\mu_0 \rho}$, the observed velocity amplitude $v \approx 20$ km s^{-1}, the spicular mass density $\rho = (2.2–40) \times 10^{-14}$ g cm^{-6}, and the magnetic field $B \approx 10$ G (De Pontieu et al. 2007). The energy flux that reaches the corona is thus on the order of $E \gtrsim 1.2 \times 10^5$ erg s^{-1} cm^{-2} for a transmission coefficient of 3%. These numerical values have also been approximately reproduced with recent 3-D radiative MHD simulations. Therefore, the upward propagating energy flux is sufficient to heat the Quiet-Sun corona and/or to power the solar wind (De Pontieu et al. 2007, 2011). Tomczyk et al. (2007) detected Alfvénic waves in the corona also, but the oscillation amplitudes turned out to be far too small (0.5 km s^{-1}) to supply the energy flux of $E \approx$ (1–2) $\times 10^5$ erg cm^{-2} s^{-1} required to heat the Quiet Sun corona. On the other hand, by using He II 304 Å and Fe IX 171 Å data from AIA/SDO, outward-propagating Alfvénic motions with periods of $\approx$ 100–500 s were detected throughout the quiescent atmosphere, which were interpreted in terms of passing Alfvénic waves that also carried sufficient energy to heat the Quiet Sun corona (McIntosh et al. 2011). In addition, CRISP/SST Hα 6562.8 Å observations revealed the ubiquitous presence of high-frequency ($\approx$ 12–42 mHz, or 20–80 s) torsional motions in thin spicular-

type structures in the chromosphere of the Quiet Sun, which by means of numerical simulations were identified as *torsional Alfvén waves*, requiring only $\lesssim$ 1% transmission to the corona to match the coronal heating requirement (Srivastava et al. 2017). Using EIS/Hinode spectral data and a magnetic field model, an energy in the range of $E \approx (1.3\text{–}5.5) \times 10^5$ erg cm^{-2} s^{-1} was found at the footpoint of Quiet-Sun loops, which amounts to more than 80% of the coronal heating requirement and was interpreted as further evidence for wave heating of the Quiet-Sun corona (Hahn and Savin 2014). Of course, besides the energy input into the corona, the dissipation mechanisms in the corona are equally important to identify in the solution of the solar heating problem.

DC heating models include stress-induced reconnection, stress-induced current cascades, or stress-induced turbulence models. The most prominent DC heating model is due to Parker, who envisioned random braiding of coronal field lines that leads through cumulative build-up of non-potential magnetic energy to magnetic reconnection events. The basic reconnection physics is similar in large-scale flares and small-scale coronal heating events (also called nanoflares), but the major issue is whether the small-scale heating events involve spatially resolved loops that can be observed and modeled individually as "monolithic elements", or whether the small-scale heating events cannot be resolved and consequently can only be modeled as a statistical phenomenon. A pioneering new result was made with the *High-resolution Coronal Imager (Hi-C)* during a rocket flight on 2012 July 11, taking images in the Fe XII 193 Å line (sensitive to a temperature of $T_e \approx 1.5$ MK), with a spatial resolution of $0.2''$ ($\approx$ 150 km). The Hi-C data show evidence of magnetic field braiding and axial twist in loops along their length (Fig. 6.13), magnetic reconnection, and subsequent heating in the low corona, while AIA/SDO with a resolution of $1.2''$ (900 km) did not resolve the braiding, but detected a flare with a temperature of $\approx$ 7 MK (Cirtain et al. 2013). In another subsequent braiding and untwisting event, a total (magnetic) free energy of $E_{tot} \approx 10^{29}$ erg was estimated. Cirtain et al. (2013) emphasize that the observed magnetic configurations imply true braiding, not just helical twisting by rotation. The braiding is driven by the ubiquitous small-scale, convection-driven motion of the photospheric feet of the magnetic field, and thus provides a true DC-like energy source for the corona (Cirtain et al. 2013). Although this particular observation reveals the unmistakable topology of braiding in the corona, it needs to be demonstrated how frequently energy releases due to braiding-induced reconnection occur, and whether their dissipated energy matches the coronal heating requirement.

Besides the method of direct imaging, a frequent approach of the coronal heating problem is the 1-D hydrodynamic modeling of the spatial heating function in coronal loops, which should tell us at least whether the data are consistent with uniform, footpoint, or apex heating (Serio et al. 1981; Priest et al. 2000). Most of the fitted data were found to be consistent with footpoint heating (e.g., Aschwanden et al. 2000; Winebarger et al. 2003). Also in the flux-tube tectonic model, the strongest heating is expected in the "carpet" near the footpoints of coronal loops, due to the preponderance of supergranular downflows in the chromosphere (Priest et al. 2002). Synthesizing recent observations, ten arguments were brought forward that yield

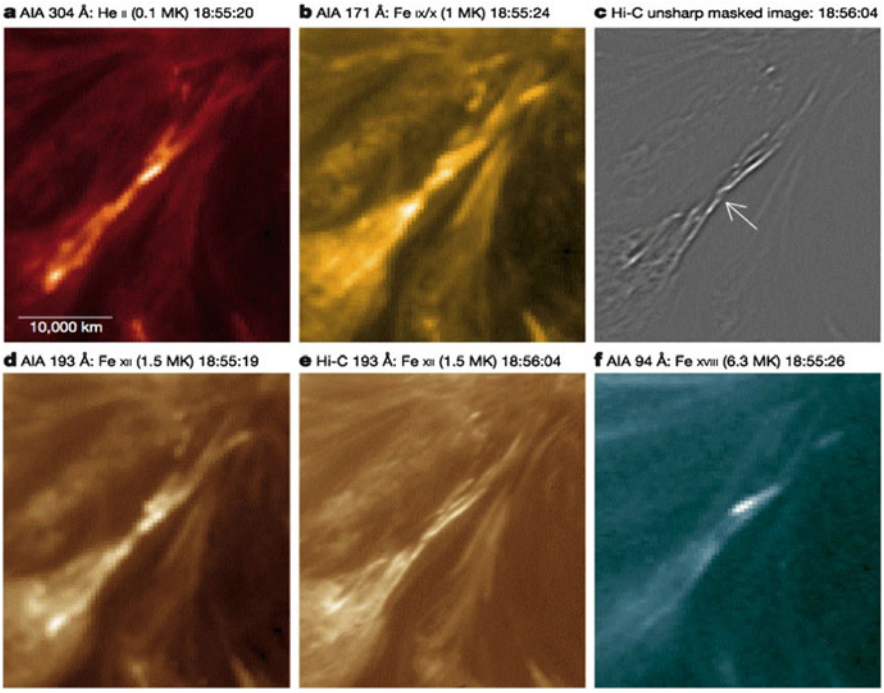

Fig. 6.13 A twisted coronal loop structure seen at different coronal temperatures by AIA and Hi-C: (**a**) AIA 304 Å, He II (0.1 MK); (**b**) AIA 171 Å, Fe IX/X (1.0 MK); (**c**) Hi-C unsharp masked; (**d**) AIA 193 Å, Fe XII (1.5 MK); (**e**) Hi-C 193 Å, Fe XII (1.5 MK); (**f**) AIA 94 Å, Fe XVIII (6.3 MK), (Cirtain et al. 2013)

strong evidence for (footpoint) heating of the corona with input from chromospheric sources (Aschwanden et al. 2007), based on: (i) the temperature evolution of coronal loops, (ii) the over-density of hot coronal loops, (iii) upflows into coronal loops, (iv) the Doppler blue-shift in coronal loops, (v) upward propagating MHD waves, (vi) the energy balance in coronal loops, (vii) the magnetic complexity in the transition region, (viii) the altitude of observed microflares and EUV nanoflares, (ix) the cross-section of elementary loops, and (x) 3-D simulations of coronal heating. More accurate atomic calculations (of Fe lines) would help also to improve the coronal temperature and heating diagnostics. Improved density measurements with EIS/Hinode in the Quiet Sun above the limb established a temperature distribution that is strongly peaked at $\approx$ 1.0 MK, but has a significant tail at higher temperatures that cannot be understood with current atomic data (Warren and Brooks 2009). A hot-temperature component in the Quiet Sun could be detectable with RHESSI, but new upper limits in the 3–200 keV range, which are substantially lower than previous ones, constrain several physical processes that could contribute to the Quiet Sun hard X-ray flux, such as coronal thin-target emission, microflares, cosmic rays, or generation of axions inside the Sun (Hannah et al. (2010)).

One theoretical concept of coronal heating processes, introduced by Eugene Parker in the 1980s, is the so-called *nanoflare model*. In the review of Klimchuk (2015), 10 key aspects of this model have been highlighted, which should be understood before we can consider the problem to be solved: (i) All coronal heating is impulsive; (ii) the details of coronal heating matter; (iii) the corona is filled with elemental magnetic strands; (iv) the corona is densely populated with current sheets; (v) the strands must reconnect to prevent an infinite build-up of stress; (vi) nanoflares repeat with different frequencies; (vii) what is the characteristic magnitude of energy release? (viii) what causes the collective behaviour responsible for loops? (ix) what are the onset conditions for energy release? (x) chromospheric nanoflares are not a primary source of coronal plasma. The biggest problem of this concept is the ambiguity and (or undetectability) of individual (unresolved) nanoflare structures.

6.8 Quiet Sun: EUV Nanoflare Energetics

The plausibility and viability of any proposed coronal heating mechanism usually has been buttressed by a back-of-the-envelope estimate of the coronal heating rate requirement, which entails an energy balance between the heating rate and the conductive and radiative loss rate. Such energy estimates are often made by assuming typical values for the involved physical parameters. Typical parameter values, however, are only valid for incoherent random processes (leading to Gaussian-like distributions), but are ill-defined for nonlinear processes with coherent growth of avalanching events (leading to scale-free, power law-like distributions). The scale-free range $[x_1, x_2]$ of power law distributions $N(x) \propto x^{-\alpha}$ is usually bound by a lower threshold x_1 (above which complete sampling is assumed), and by an upper bound x_2 (which is given by the largest observed event). The total energy contained in a distribution can then conveniently be obtained by integrating the power law distributions over the scale-free range (also called *inertial range*). The peak of the power law distribution is usually found to be close to the threshold of complete sampling, rather than being a typical (mean) value of a Gaussian random distribution. Size distributions (also called *frequency distributions* or *occurrence rate distributions*) of different data sets, should only be compared for equal threshold values x_1 and equal time ranges $[t_1, t_2]$ of the data sets, unless they are properly normalized to the same total number of events and the same threshold. Substantial progress has been accomplished over the last three decades by quantifying the (power law-like) size distributions of Quiet Sun small-scale events (or EUV nanoflares), rather than estimating (ill-defined) typical values.

Before we review the statistics and energetics of small-scale events in the Quiet Sun, we have to clarify the nomenclature of the so-called *nanoflare* events. There is an observational and a theoretical meaning of this term. The observations refer to *large flares* in the energy range of $E \approx 10^{30}$–10^{33} erg, to *microflares* in the energy range of $E \approx 10^{27}$–10^{30} erg, and to *nanoflares* in the energy range of $E \approx 10^{24}$–10^{27} erg (Fig. 6.14). While large flares are detected in hard X-rays,

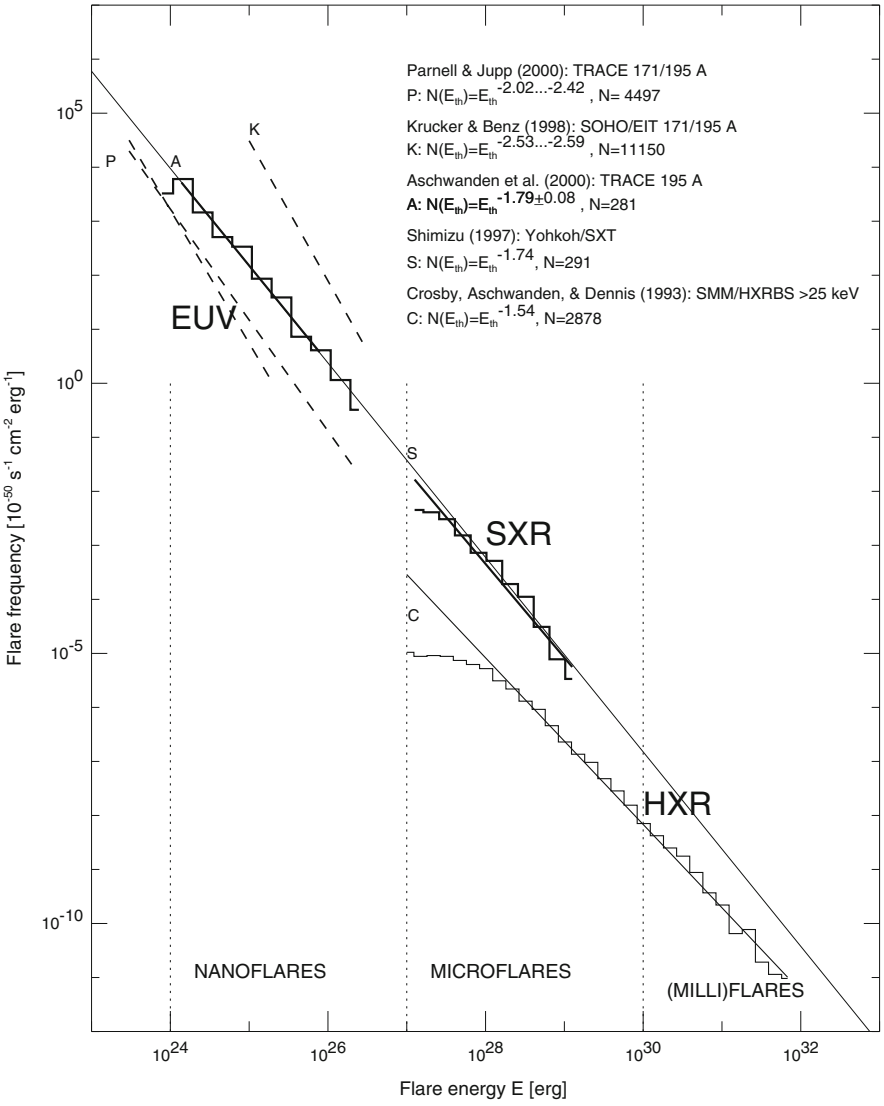

Fig. 6.14 Composite flares frequency distribution in a normalized scale in units of 10^{50} flares per time unit (s^{-1}), and energy unit (erg^{-1}). The diagram includes EUV flares analyzed in Krucker and Benz (1998), Parnell and Jupp (2000), Aschwanden et al. (2000), and compared with soft X-ray brightenings (Shimizu 1997), and hard X-ray flares (Crosby et al. 1993). All flare energies are specified in terms of the thermal energy $E_{th} = 3n_e k_B T_e V$, except for the hard X-ray flares. An overall power law slope of $\alpha = 1.8$ is indicated, extending over the entire energy domain of 10^{24}–10^{32} erg (Aschwanden et al. 2000)

microflares are seen in soft X-rays, and nanoflares in EUV wavelengths. These nanoflares observed in EUV show all characteristics of large flares (cooling delay, small post-flare loops, etc), and appear to consist of resolved flare loops with widths of $w \approx 1.0$–1.5 Mm (Krucker and Benz 1998; Parnell and Jupp 2000; Aschwanden et al. 2000). On the other side, the term *"nanoflares"* has also been used in the theoretical concept of Eugene Parker (1988), who estimates an energy of $E \approx 10^{24}$ erg for a "typical" small-scale magnetic reconnection event that smoothes out the apparent braiding of coronal loops. The major discrepancy between these two definitions of *nanoflare events* is that the observational definition is based on resolved (post-flare) loop structures, while the theoretical definition hypothesizes unresolved loop strands, so it is an issue of resolved versus unresolved structures. In order to disambiguate this dual definition of the term *nanoflares* we will use the two terms *"EUV nanoflares"* and *"Parker nanoflares"*, with the understanding that the former is based on resolved elementary loops (being observational structures), while the latter assumes unresolved elementary loops (being a theoretical hypothesis).

Three statistical studies on the energy size distribution of *EUV nanoflares* in the Quiet Sun were conducted by Krucker and Benz (1998), Parnell and Jupp (2000), and Aschwanden et al. (2000). All three studies selected EUV data (EIT/SOHO, TRACE), a field-of-view in the Quiet Sun (away from active regions), used similar (but independently developed) automated event detection algorithms, and obtained similar energy ranges, but somewhat different power law slopes α of the energy size distribution (Fig. 6.14): $\alpha \approx 2.3$–2.6 (Krucker and Benz 1998); $\alpha \approx 2.4$–2.6 (Parnell and Jupp 2000); $\alpha \approx 1.8$ (Aschwanden et al. 2000). The differences in these power slopes can easily be explained by a number of systematic effects, such as: the selection of events, the model of the line-of-sight depth, and/or different detection thresholds, etc. (Aschwanden et al. 2000; Benz and Krucker 2002). Taking the fractal geometry of the EUV nanoflare volume and a broader temperature coverage of EUV and soft X-ray wavelengths into account, the slope of the power law distribution of EUV nanoflare energies flattens to $\alpha \approx 1.54 \pm 0.03$ (Aschwanden and Parnell 2002). There is a critical power law slope value of $\alpha_{crit} = 2$ that implies divergence of the integral at the lower (or upper) end of the size distribution, depending on whether the slope is larger (or smaller) than this critical value. If this criterion is applied, there is more energy in EUV nanoflares than in large flares for measurements of $\alpha > 2$ (Krucker and Benz 1998; Parnell and Jupp 2000), and vice versa for $\alpha < 2$ (Aschwanden et al. 2000). However, the extrapolation of the power law size distribution to unobserved energies that are many orders of magnitude smaller remains questionable (Benz and Krucker 2002), and may invalidate the importance of nanoflare heating of the Quiet Sun corona by unresolved Parker nanoflares. Parnell and Jupp (2000) find that EUV nanoflares occur in 16% of the solar surface only, in regions with the brightest EUV emission, which are presumably the regions connected to the strongest magnetic fields (i.e., active regions), which does not explain *Parker nanoflare* heating in the EUV-faint parts of the Quiet Sun. Harrison et al. (2003) proposed a unification of Quiet-Sun transient-event phenomena, for instance blinkers, network flares, cell brightenings, and EUV brightenings appear to have the same physical characteristics, which could be added

Table 6.2 Frequency distributions of small-scale phenomena observed in Quiet Sun regions (Aschwanden et al. 2000)

Phenomenon	Number of events N	Powerlaw slope α_E	Energy range E_1, E_2 10^{24} [erg]	Total flux F [erg cm^{-2} s^{-1}]
EUV transients, EIT, 171+195[a]	233	2.45 ± 0.15	10–300	0.7×10^5
EUV transients, EIT 195[b]	228	1.35 ± 0.20	1–100	...
EUV transients, EIT 195[c]	277	1.45 ± 0.20	10–100	...
Nanoflares, TRACE, 171+195[d]	5131	2.48 ± 0.11	0.3–60	0.2×10^5
Nanoflares, TRACE+SXT[e]	281	1.53 ± 0.02	10–10^6	0.5×10^5
Blinkers, CDS, O V[f]	790	1.34 ± 0.08	0.01–0.3	...
Explosive ev., SUMER C III[g]	3403	2.8 ± 0.1	0.05–2	0.45×10^5
Explosive ev., SUMER Ne IV[g]	2505	2.8 ± 0.1	0.6–10	0.16×10^5
Explosive ev., SUMER O VI[g]	5531	3.3 ± 0.4	0.1–2	0.79×10^5
Explosive ev., SUMER Ne VIII[g]	2907	2.8 ± 0.5	0.06–1	0.03×10^5
Quiet Sun heating requirement				3.0×10^5

[a]Krucker and Benz (1998); [b]Berghmans et al. (1998); [c]Berghmans and Clette (1999); [d]Parnell and Jupp (2000) [corrected for a factor of 100 in original paper]; [e]Aschwanden et al. (2000); [f]Brkovic et al. (2001); [g]Winebarger et al. (2002)

to the EUV nanoflare events and this way boost the overall energy input into the Quiet Sun corona.

In Table 6.2 we compile frequency distributions of small-scale phenomena that have been reported from the Quiet Sun and calculate their total energy flux F based on the observed energy ranges $[E_1, E_2]$ and the power law slopes α_E. EUV transients, nanoflares and microflares generally are found in the energy range of $E \approx 10^{24}$–10^{26} erg and the integrated flux over the entire observed frequency distribution lies in the range of $F \approx (0.5 \pm 0.2) \times 10^5$ erg^{-1} cm^{-2} s^{-1}, which makes up about one sixth of the total heating requirement of the Quiet corona, roughly covering the radiative losses in the Quiet Sun corona. A similar flux was also measured for explosive events in C III, Ne IV, and O VI (Winebarger et al. 2002), which fits into the picture that explosive events and nanoflares are probably controlled by the same physical process as a magnetic reconnection process in the transition region. This conclusion is also supported by the comparable amounts of thermal plasma inside the transition region (as detected in the cooler EUV lines in C III, Ne IV, and O VI) as well as in the lower corona (in the hotter EUV lines of Fe IX/X and Fe XII). Other phenomena such as blinkers carry several orders of magnitude less energy ($E \approx 10^{22}$–3×10^{23}; Brkovic et al. 2001), and thus seem to be energetically less important for coronal heating.

6.9 Quiet Sun: Fluxtube Braiding

The theoretical concept of fluxtube braiding as a coronal heating mechanism of the Quiet Sun, introduced by Parker (1972) as *topological dissipation and the small-scale fields in turbulent gases*, became testable once the first 3-D MHD numerical simulations (Gudiksen and Nordlund 2002, 2005a,b) of a realistic-looking corona, displaying a number of loop-like structures, became available (Peter et al. 2004).

Of course, the efficiency of fluxtube braiding completely depends on how the system is driven, and how the time-dependent boundaries of the computation box are defined. In the first simulations (Gudiksen and Nordlund 2002, 2005a,b; Peter et al. 2004), the initial magnetic field was obtained from a potential field extrapolation of a MDI/SOHO magnetogram of active region NOAA 9114. The lower boundary is stressed by a time-dependent velocity field, constructed from a Voronoi tesselation that reproduces the granulation pattern (Schrijver et al. 1997), while the velocity field reproduces the geometric pattern as well as the amplitude power spectrum of the velocity and vorticity (Peter et al. 2004). In this MHD simulation, the braiding of the magnetic field by the photospheric motions rapidly produces an intermittent corona in both time and space with a typical temperature of $\approx$ 1 MK, during the whole simulated time span of $\approx$ 50 min. The time- and space-averaged heating function decreases exponentially with height, producing a heat input of $E \approx (2\text{–}8) \times 10^6$ erg cm^{-2} s^{-1} that is sufficient to heat the corona (in the chosen active region, and supposedly in Quiet Sun regions also). Using the electron density, temperature, and velocity from the MHD model, the emissivity for a number of UV and EUV emission lines could be synthesized, which matched the typical observed values, so that Peter et al. (2004) concluded that the fluxtube braiding mechanism is a prime candidate for being the dominant heating process of the magnetically closed corona of the Sun and solar-like stars. More advanced simulations of coronal heating through footpoint braiding have been conducted by Hansteen et al. (2015), including a convection zone, where granulation and associated flows are driven by self-consistent convection. On smaller scales, heating is concentrated in current sheets with widths set by the numerical resolution.

Following Parker's braiding concept, the plasma volumes of coronal loops should repeatedly be spliced, leading to an increase of loop width with time, with a diffusion coefficient of 93 ± 9 km^2 s^{-1} (Schrijver 2007), which matches the dispersion coefficient of the granular random walk up to several hours. Consequently, loop width observations indicate that granular braiding is statistically countered by frequent coronal (interchange) reconnection events, which in turn explains the general absence of entangled coronal field structures in the quiescent corona (Schrijver 2007).

Other measures of the degree of braiding involves the *squashing factor* Q (a property of magnetic field line mapping) and *quasi-separatrix layers (QSL)*, for which it is found that the maximum values of Q increase exponentially, as the degree of braiding of the magnetic field is increased, while myriads of thin QLSs form, and thus QSLs are not good predictors or current features in this class of braided fields

(Wilmot-Smith et al. 2009a). An analytical braiding model with parallel electric fields shows that loss of equilibrium is an inevitable consequence of the braiding process, probably via magnetic reconnection events (Wilmot-Smith et al. 2009b).

The dynamics of a braiding loop pair has been explored with a resistive 3-D MHD code, starting with an initial near force-free field, and leading to a long-wavelength instability and formation of two thin current sheets, including an elliptic magnetic field structure about the reconnection site, and resulting in an untwisting of the global field (Wilmot-Smith et al. 2010). A myriad of thin current layers form via a cascade process, triggering multiple reconnection events, and finally ending in a non-linear force-free field of two flux tubes of oppositely-signed twist embedded in a uniform background field (Pontin et al. 2011). Similar simulations leading to heating of the braided loops are described in Wilmot-Smith et al. (2011), Wilmot-Smith (2015), Pontin and Hornig (2015).

The braiding of coronal loop strands can be modeled in terms of a self-organized criticality model, similar to a forest fire model, in which the frequency distributions of coherent braid sequences as well as flare energies follow power law distributions (Berger and Asgari-Targhi 2009, 2015). A similar cut-and-splice model of loop strands has been modeled by Morales and Charbonneau (2008), which mimics the braiding of loop strands and reproduces the power law distributions typical for self-organized criticality models. It is suggested that the braiding-associated reconnection in the corona can be understood in terms of a self-organized criticality model driven by convective rotational motions, similar to those observed at the photosphere (Knizhnik et al. 2018).

What observational tests can be designed for braiding loops? A more specific question is: if energy release occurs in a coronal loop containing braided magnetic flux, should we expect a clearly observable signature in emissions? Pontin et al. (2017) attempt to answer this question by using MHD simulations and forward modeling of synthesized EUV images (Fig. 6.15). They demonstrate that the presence of braided magnetic field lines does not guarantee a braided appearance to the observed intensities. However, in all cases they considered, the evolution of the braided loop is accompanied by localized heating regions as the loop relaxes. An inspection of the Hi-C movies that contain braided structures (Cirtain et al. 2013) reveals emission patterns indicative of braiding on multiple spatial scales (Pontin et al. 2017). There is also a superposition effect that doubles the (optically thin) EUV brightness at the intersections of two equally bright crossing loop segments, which needs to be taken into account in forward-modeling and data analysis of braided loops. Another important distinction that needs to be folded into 3-D modeling of loops is twisting versus braiding geometries (Prior and Yeates 2016a). The electric current structures of the final states of simulated flux ropes differ significantly between the braided field (which has a diffuse nature), and the twisted field (which displays a clear sigmoid), and could be observable (Prior and Yeates 2016a,b). In addition, quasi-periodic flows within a velocity range of 13–185 km s^{-1} have been detected in braided structures, possibly outflows from reconnection sites (Pant et al. 2015), which can be compared with MHD simulations.

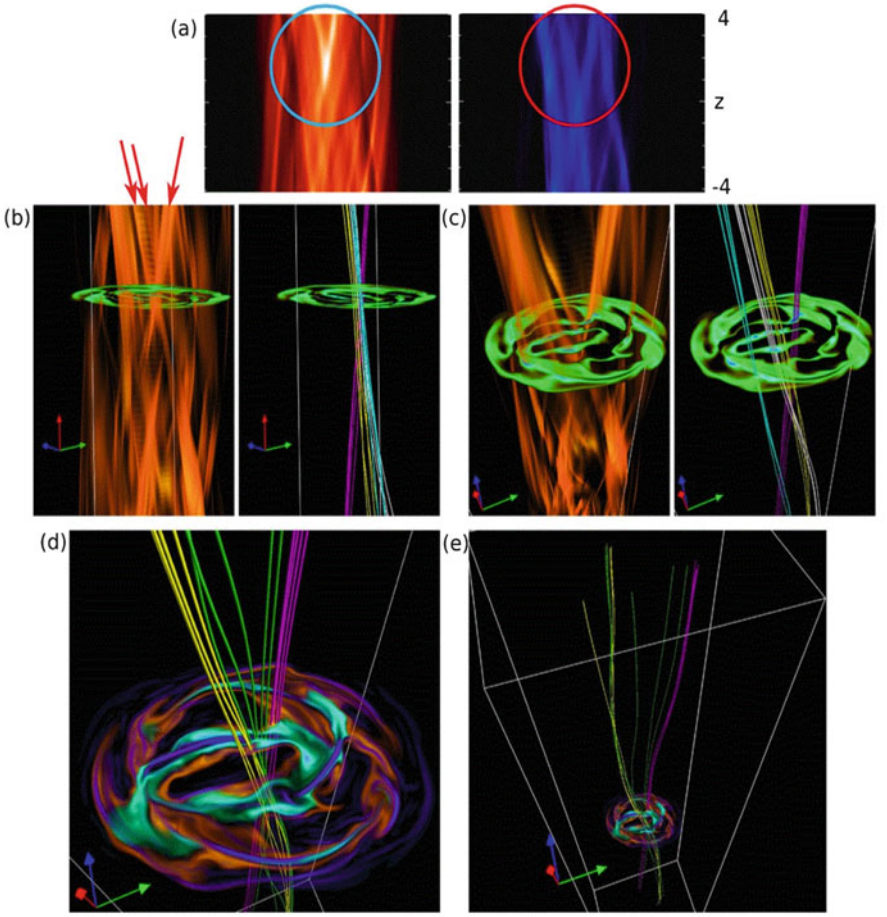

Fig. 6.15 Braiding simulation: (**a**) Close-up of a braiding structure from a synthesized EUV image in Fe XII 193 Å (red-orange) and Fe XV 284 Å (blue); (**b–e**) Different aspect angles and field-of-views. The shading in the cross-sections show regions of Fe XII emission (orange), Fe XV (cyan), and current density (purple), (Pontin et al. 2017)

Estimates of the energy input from magnetic braiding have been inferred within a range of 10^6–3.5×10^8 erg cm^{-2} s^{-1}, based on SP/Hinode data (Yeates et al. 2014). Applying a nonlinear force-free magnetic field reconstruction to the braided structure observed by Cirtain et al. (2013) yields a free energy that is about 100 times larger than estimated previously, which strengthens the possibility of the active region corona being heated by field line braiding (Thalmann et al. 2014).

6.10 Quiet Sun: Radio Emission

A recent review on radio emission of the Quiet Sun and active regions is provided in Shibasaki et al. (2011). Solar radio emission is traditionally divided into a background component (Quiet Sun), a slowly-varying component (associated mostly with active regions), and a sporadic (flare-related) burst component, but new measurements reveal considerable variability even for the Quiet Sun component. With the high-resolution observations of ALMA, even the background component became more dynamic, of course. Most of the Quiet Sun emission is produced by thermal bremsstrahlung in *local thermodynamic equilibrium (LTE)*, originating in chromospheric heights. An overview of contribution functions in the wavelengths from $\lambda = 3$ cm down to $\lambda = 70$ nm is shown in Fig. 6.16. The height-dependent temperatures $T_e(h)$, densities $n_e(h)$, and free-free opacities $\tau(h)$ have been calculated from an atmospheric model (Sect. 5.1), such as the semi-empirical Avrett and Loeser (2008) model (Fig. 6.16, red curves), or the Fontenla et al. (2007, 2009) models, which describe the average Quiet Sun chromosphere and transition region up to $T = 1.6$ MK and the Quiet Sun spectrum in the wavelength range of $\lambda = 0.04$–40 mm. Most of the radio emission at $\lambda = 3$ cm and shorter wavelengths originates below the transition region, with a small contribution from the transition region itself and no contribution from the corona. The brightness temperature as a function of wavelength has been calculated by Loukitcheva et al. (2004), based on static atmospheric models (Avrett and Loeser 2008), as well as based on the dynamic simulations of Carlsson and Stein (2002) (Fig. 6.16, bottom right panel). Their conclusion was that the dynamic picture of the solar internetwork chromosphere is consistent with the currently available mm and sub-mm brightness observations. Extending the chromospheric spectrum to the corona (say up to a wavelength of $\lambda = 20$ cm) requires a two-component model with an optically thick chromosphere and an isothermal corona. In order to match the radio polar brightening observed by the Nobeyama radioheliograph at 17 GHz, a spicular component with holes and faculae is needed (Selhorst et al. 2005, 2010). Modeling of the microwave polar brightening and its solar cycle variation has remained to be a persistent problem because of the sensitivity of the gyroresonance component to the magnetic field (Gopalswamy et al. 2012; Kim et al. 2017; Shimojo et al. 2017a).

A powerful new instrument that faciliates chromospheric modeling with unprecedented high spatial resolution is the *Atacama Millimeter/Submillimeter Array (ALMA)* in Chile (Wooten and Thompson 2009). ALMA consists of up to 66 antennas, configurable on baselines from 150 m to 15 km, and operates in the frequency range of 84–950 GHz. ALMA became operational during 2016 and produced already a number of studies. First high-resolution synthesized images were obtained during the solar-commissioning campaign in December 2015 (Shimojo et al. 2017b). White et al. (2017) used a fast-scanning method to make single-dish maps of the full Sun (Fig. 6.17). A first comparison of millimeter continuum maps from ALMA with UV maps in Mg II from IRIS demonstrated a detailed correspondence down to the fine structure of penumbral fibrils, but revealed a temperature difference

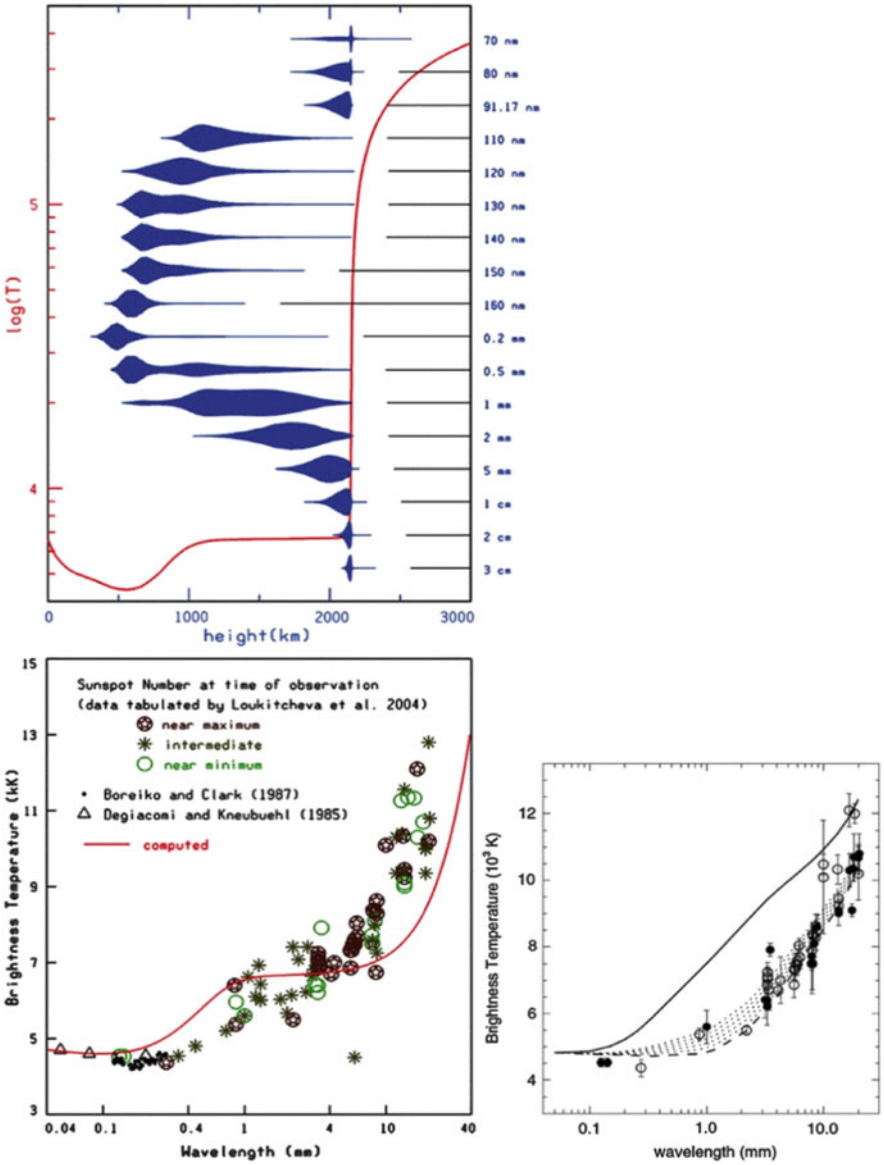

Fig. 6.16 Contribution functions at microwave and millimeter wavelengths according to the model of Avrett and Loeser (2008) (top panel), the corresponding spectrum (bottom left panel), and spectra computed by Loukitcheva et al. (2004) (bottom right), based on the FAL model F in networks (solid line), and based on the dynamic simulations by Carlsson and Stein (2002) (dotted lines). Data points near solar maximum (minimum) are represented with open (filled) circles, (Shibasaki et al. 2011)

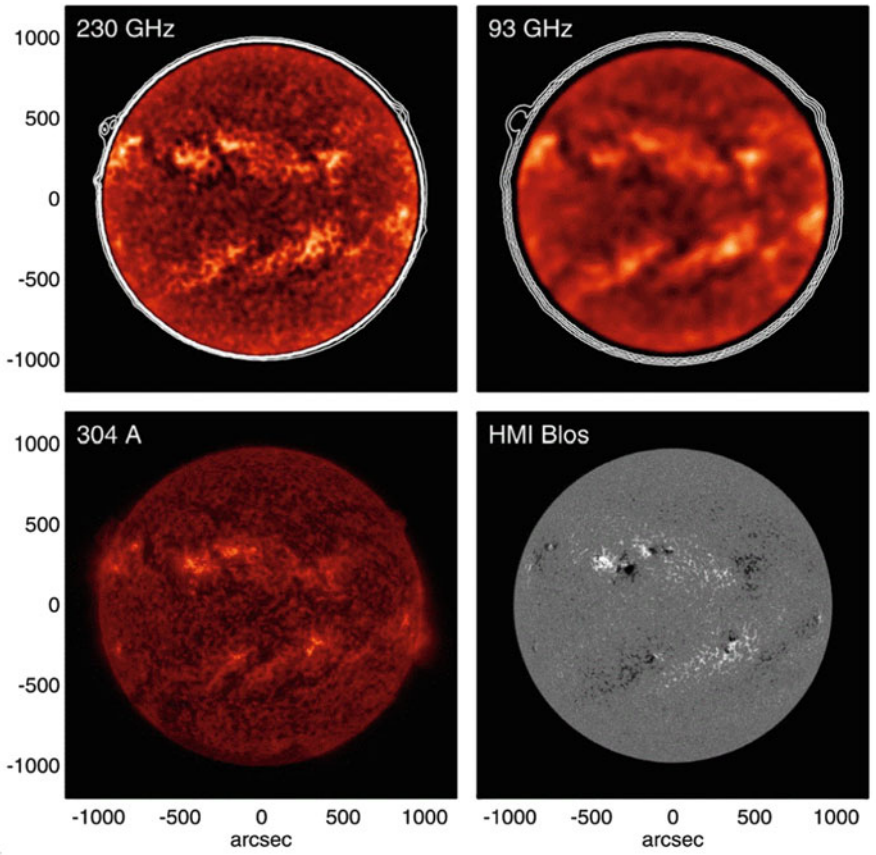

Fig. 6.17 ALMA fast-scanning observations of the Sun on 17 December 2015 at 230 GHz (5300–7400 K) and 93 GHz (6700–8800 K) (top panels), compared with a He II 304 Å AIA/SDO images (bottom left panel) and a HMI/SDO magnetogram (lower right panel), (White et al. 2017)

of 35% between the radio brightness temperature and the Mg II temperature (Bastian et al. 2017), which is currently re-analyzed. For the first time, millimeter observations of sunspots have resolved the umbral/penumbral brightness structure at chromospheric heights, revealing a temperature difference of $\approx$ 600 K between the inner part of the umbra and the surrounding Quiet Sun (Loukitcheva et al. 2017b). One strategy is to use the circular polarization of free-free emission to infer the chromospheric magnetic field. 3-D non-LTE radiative MHD simulations of the Quiet Sun have been carried out to test the chromospheric field diagnostics from free-free radiation at mm and sub-mm wavelengths (Loukitcheva et al. 2017a). The most recent review on solar science carried out with ALMA is given in Wedemeyer et al. (2016).

Another new radio interferometer that came online is the *Allen Telescope Array (ATA)*, a radio interferometer near Hat Creek, California, consisting of 42 antennas configured with baselines up to 300 m. First full-Sun maps were obtained in microwave frequencies (1.43–6.0 GHz) during 2009–2010, produced for the first time without mosaic assembling (Saint-Hilaire et al. 2012).

References

(6.1) Solar Eclipses

Alzate, N., Habbal, S.R., Druckmüller, M., et al. 2017, *Dynamics of large-scale coronal structures as imaged during the 2012 and 2013 total solar eclipses*, ApJ 848, 84, [1 c, 1 c/y].

Bleeker, J.A.M., Geiss, J., and Huber, M.C.E. (eds.) 2001. *The Century of Space Science*, p.220, Kluwer Academic Publishers, Dordrecht.

Byhring, H.S., Cranmer, S.R., Lie-Svendsen, O., et al. 2011, *Modeling iron abundance enhancements in the slow solar wind*, ApJ 732, 119, [5 c, 1 c/y].

Druckmüller, M., Habbal, S.R., and Morgan H., 2011, *Discovery of new class of coronal structures in white light eclipse images*, ApJ 785, 14, [14 c, 4 c/y].

Druckmüller, M., Habbal, S.R., Alzate, N., et al. 2017, *Tethered prominence-CME systems captured during the 2012 November 13 and 2013 November 3 total solar eclipses*, ApJ 851, L41, [1 c, 1 c/y].

Druckmüllerova, H., Morgan, H., and Habbal, S.R. 2011, *Enhancing coronal structures with the Fourier normalizing-radial-graded filter*, ApJ 737, 88, [9 c, 1 c/y].

Habbal, S.R., Morgan, H., Johnson, J., et al. 2007, *Localized enhancements of Fe^{+10} density in the coronal as observed in Fe XI 789.2 nm during the 2006 March 29 total solar eclipse*, ApJ 663, 598, [22 c, 2 c/y].

Habbal, S.R., Druckmüller, M., Morgan, H. et al. 2010a, *Mapping the distribution of electron temperature and Fe charge states in the corona with total solar eclipse observations*, ApJ 708, 1650, [34 c, 5 c/y].

Habbal, S.R., Druckmüller, M., Morgan, H., et al. 2010b, *Total solar eclipse observations of hot prominence shrouds*, ApJ 719, 1362, [44 c, 6 c/y].

Habbal, S.R., Druckmüller, M., Morgan, H. et al. 2011, *Thermodynamics of the solar corona and evolution of the solar magnetic field as inferred from the total eclipse observations of 2010 July 11*, ApJ 734, 120, [35 c, 5 c/y].

Habbal, S.R., Morgan, H., Druckmüller, M. et al. 2013, *Probing the fundamental physics of the solar corona with lunar solar occultation observations*, SoPh 285, 9, [12 c, 3 c/y].

Habbal, S.R., Morgan, Y., and Druckmüller, M. 2014, *Exploring the prominence-corona connection and its expansion into the outer corona using total solar eclipse observations*, ApJ 793, 119, [5 c, 1 c/y].

Hanaoka, Y., Kikuta, Y., Nakazawa, J., et al. 2012, *Accurate measurements of the brightness of the white-light corona at the total solar eclipses on 1 August 2008 and 22 July 2009*, SoPh 279, 75, [8 c, 1 c/y].

Lamy, P., Prado, J.Y., Floyd, O., et al. 2015, *A novel technique for measuring the solar radius from eclipse light curves - Results for 2010, 2012, 2013, and 2015*, SoPh 290, 2617, [4 c, 2 c/y].

Nandy, D., Bhowmik, P., Yeates, A.R., et al. 2018, *The large-scale coronal structure of the 2017 August 21 great American eclipse: An assessment of solar surface flux transport model enabled predictions and observations*, ApJ 853, 72.

Skomorovsky, V.I., Trifonov, V.D., Mashnich, G.P., et al. 2012, *White-light observations and polarimetric analysis of the solar corona during the eclipse of 1 August 2008*, SoPh 277, 267, [9 c, 2 c/y].

(6.2) Quiet Sun: Flows and Jets

De Pontieu, B., Hansteen, V.H., Rouppe van der Voort, L. 2007a, *High-resolution observations and modeling of dynamic fibrils*, ApJ 655, 624, [143 c, 14 c/y].
De Pontieu, B., McIntosh, S.W., Hansteen, V.H., et al. 2007b, *A tale of two spicules: The impact of spicules on the magnetic chromosphere*, PASJ 59, S655, [235 c, 22 c/y].
Filippov, B., Koutchmy, S., and Vilinga, J. 2007, *On the dynamic nature of the prolate solar chromosphere: Jet formation*, A&A 464, 1119, [12 c, 1 c/y].
Hansteen, V.H., De Pontieu, B., Rouppe van der Voort, L. 2006, *Dynamic fibrils are driven by magneto-acoustic shocks*, ApJ 647, L73, [194 c, 17 c/y].
Hong, J., Jiang, Y., Zheng, R., et al. 2011, *A micro CME associated blowout EUV jet*, ApJ 738, L20, [43 c, 7 c/y].
Innes, D.E., Genetelli, A., Attie, R., et al. 2009, *Quiet Sun mini-CMEs activated by supergranular flows*, A&A 495, 319, [47 c, 6 c/y].
Innes, D.E. and Teriaca, L. 2013, *Quiet Sun explosive events: Jets, Splashes, and Eruptions*, SoPh 282, 453, [14 c, 3 c/y].
Lee, C.Y., Chae, J.C., and Wang, H. 2000, *Dynamical characteristics of small-scale Hα upflow events on the Quiet Sun*, ApJ 545, 1124, [20 c, 1 c/y].
Martinez Pillet, V., del Toro Iniesta, J.C., and Quintera Noda C. 2011, *Ubiquitous Quiet-Sun jets*, A&A 530, A111, [17 c, 3 c/y].
McIntosh, S.W. and De Pontieu, B. 2009, *High-speed transition region and coronal upflows in the Quiet Sun*, ApJ 707, 524, [63 c, 7 c/y].
Peter, H., Brkovic, A. 2003, *Explosive events and transition region blinkers: Time variability of non-Gaussian Quiet-Sun EUV spectra*, A&A 403, 287, [14 c, 1 c/y].
Potts, H.E., Khan, J.I., and Diver, D.A. 2007, *Small-scale energy release driven by supergranular flows on the Quiet Sun*, SoPh 245, 55, [7 c, 0.7 c/y].
Rouppe van der Voort, L.H., De Pontieu, B., Hansteen, V.H., et al. 2007, *Magnetoacoustic shocks as a driver of Quiet-Sun mottles*, ApJ 660, L169, [69 c, 6 c/y].
Rubio da Costa, E., Solanki, S.K., Danilovic, S., et al. 2015, *Center-to-limb properties of small, photospheric Quiet-Sun jets*, A&A 574, A95, [3 c, 1 c/y].
Shimizu, T., Lites, B.W., Katsukawa, Y., et al. 2008, *Frequent occurrence of high-speed local mass downflows on the solar surface*, ApJ 680, 1467, [41 c, 4 c/y].
Shimojo, M., Narukage, N., Kano, R., et al. 2007, *Fine structures of solar X-ray jets observed with the X-Ray Telescope (XRT) aboard Hinode*, PASJ 59, S745, [42 c, 4 c/y].
Tian, H., McIntosh, S.W., Habbal, S.R., et al. 2011, *Observation of high-speed outflow on plume-like structures of the Quiet Sun and coronal holes with SDO/AIA*, ApJ 736, 130, [52 c, 8 c/y].
Wyper, P.F. and DeVore, C.R. 2016, *Simulations of solar jets confined by coronal loops*, ApJ 820, 77, [9 c, 6 c/y].
Zeng, Z., Chen, B., Haisheng J., et al. 2016, *Resolving the fan-spine reconnection geometry of a small-scale chromospheric jet event with the New Solar Telescope (NST)*, ApJ 819, L3, [5 c, 3 c/y].

(6.3) Quiet Sun: Cyclones and Tornadoes

Levens, P.J., Labrosse, N., Fletcher, L., et al. 2015, *A solar tornado observed by EIS. Plasma diagnostics*, A&A 582, A27, [13 c, 5 c/y].
Li, X., Morgan, H., Leonard, D., et al., 2012, *A solar tornado observed by AIA/SDO: Rotational flow and evolution of magnetic helicity in a prominence cavity*, ApJ 752, L22, [67 c, 12 c/y].
Luna, M., Moreno-Insertis, F., and Priest, E. 2015, *Are tornado-like magnetic structures able to support solar prominence plasma ?* ApJ 808, L23, [10 c, 4 c/y].
Magara, T., An, J.M., Lee, H., et al. 2012, *Chromospheric running wave from a solar cyclone produced through the emergence of a twisted magnetic flux tube*, PASJ 64, L4.

Mghebrishvili, I., Zaqarashvili, T.V., Kukhianidze, V., et al. 2015, *Dynamics of a solar prominence tornado observed by SDO/SIS on 2012 November 7–8*, ApJ 810, 89, [4 c, 2 c/y].
Panasenco, O., Martin, S.F., and Velli, M. 2014, *Apparent solar tornado-like prominences*, SoPh 289, 603, [32 c, 9 c/y].
Panesar, N.K., Innes, D.E., Tiwari, S.K., et al. 2013, *A solar tornado triggered by flares ?* A&A 549, A105, [30 c, 7 c/y].
Schmieder, B., Mein, P., Mein, N., et al. 2017, *Hα shifts in a tornado in the solar corona*, A&A 597, A109, [5 c, 10 c/y].
Su, Y., Wang, T., Veronig, A., et al., 2012, *Solar magnetized "tornadoes": Relation to filaments*, ApJ 756, L41, [50 c, 9 c/y].
Su, Y., Gömöry, P., Veronig, A., et al. 2014, *Solar magnetized tornadoes: Rotational motion in a tornado-like prominence*, ApJ 785, L2, [24 c, 7 c/y].
Wang, W., Liu, R., and Wang, Y. 2017, *Tornado-like evolution of a kink-unstable solar prominence*, ApJ 834, 38, [3 c, 3 c/y].
Wedemeyer-Böhm, S. and Rouppe van der Voort, L. 2009, *Small-scale swirl events in the Quiet-Sun chromosphere*, A&A 507, L9, [79 c, 9 c/y].
Wedemeyer-Böhm, S., Scullion, E., Steiner, O., 2012, *Magnetic tornadoes as energy channels into the solar corona*, Nature 486, 505, [157 c, 29 c/y].
Wedemeyer, S., Scullion, E., Rouppe van der Voort, L. et al., 2013, *Are giant tornadoes the legs of solar prominences ?* ApJ 774, 123, [39 c, 9 c/y].
Wedemeyer, S. and Steiner, O. 2014, *On the plasma flow inside magnetic tornadoes on the Sun*, PASJ 66, S108, [15 c, 4 c/y].
Xu, X., Zhang, J., Li, T., et al. 2014, *Homologous cyclones in the Quiet Sun*, ApJ 782, L15, [4 c, 1 c/y].
Yang, Z., Tian, H., Peter, H., et al. 2018, *Two solar tornadoes observed with the IRIS*, ApJ 852, 79, [1 c, 1 c/y].
Zhang, J. and Liu, Y. 2011, *Ubiquitous rotating network magnetic fields and EUV cyclones in the Quiet Sun*, ApJ 741, L7, [42 c, 6 c/y].

(6.4) Quiet Sun: Magnetic Field

Aschwanden,M.J., Reardon,K., and Jess,D.B. 2016, *Tracing the chromospheric and coronal magnetic field with AIA, IRIS, IBIS, ROSA*, ApJ 826, 61, [5 c, 3 c/y].
Buehler, D., Lagg, A., Solanki, S.K. 2013, *Quiet Sun magnetic fields observed by Hinode: Support for a local dynamo*, A&A 555, A33, [35 c, 8 c/y].
Close, R.M., Parnell, C.E., Longcope, D.W. et al. 2004, *Recycling of the solar corona's magnetic field*, ApJ 612, L81, [52 c, 4 c/y].
Close, R.M., Parnell, C.E., and Priest, E.R. 2005, *Separators in 3-D Quiet-Sun magnetic fields*, SoPh 225, 21, [32 c, 2 c/y].
DeRosa, M.L., Wheatland, M.S., Leka, K.D., et al. 2015, *The influence of spatial resolution on nonlinear force-free modeling*, ApJ 811, 107, [24 c, 10 c/y].
Hagenaar, H.J. 2001, *Ephemeral regions on a sequence of full-disk MDI magnetograms*, ApJ 555, 448, [153 c, 9 c/y].
Long,D.M., Williams,D.R., Régnier,S., et al. 2013, *Measuring the magnetic field strength of the Quiet solar corona using EIT waves*, SoPh 288, 567, [15 c, 3 c/y].
Longcope, D.W. 2005, *Topological methods for the analysis of solar magnetic fields*, LRSP 2, 7, [107 c, 9 c/y].
Longcope, D.W. and Parnell, C.E. 2009, *The number of magnetic null points in the Quiet Sun corona*, SoPh 254, 51, [47 c, 6 c/y].
Mackay, D.H. and Yeates, A.R. 2012, *The Sun's global photospheric and coronal magnetic fields: Observations and Models*, LRSP 9, 6, [69 c, 12 c/y].

Orozco Suarez, D., Bellot Rubio, L.R., Del Toro Iniesta, J.C., et al. 2007, *Quiet-Sun internetwork magnetic fields from the inversion of Hinode measurements*, ApJ 670, L61, [162 c, 15 c/y].
Priest, E.R., Heyvaerts, J.F., Title, A.M. 2002, *A flux-tube tectonics model for solar coronal heating driven by the magnetic carpet*, ApJ 576, 533, [152 c, 10 c/y].
Régnier, S., Parnell, C.E., and Haynes, A.L. 2008, *A new view of Quiet-Sun topology from Hinode/SOT*, A&A 484, L47, [44 c, 5 c/y].
Schrijver, C.J. and van Ballegooijen, A.A. 2005, *Is the Quiet Sun corona a quasi-steady, force-free environment?* ApJ 630, 552, [36 c, 3 c/y].
Tadesse, T., Wiegelmann, T., and MacNeice, P.J. 2015, *Effect of the size of the computational domain on spherical nonlinear force-free modeling of a coronal magnetic field using SDO/HMI data*, SoPh 290, 1159, [1 c, 0.4 c/y].
Weinzierl, M., Yeates, A.R., Mackay, D.H., et al. 2016, *A new technique for the photospheric driving of non-potential solar coronal magnetic field simulations*, ApJ 823, 55, [7 c, 3 c/y].
Wiegelmann, T. and Solanki, S.K. 2004, *Similarities and differences between coronal holes and Quiet Sun: Are loop statistics the key?* SoPh 225, 227, [34 c, 3 c/y].
Wiegelmann, T., Solanki, S.K., Borrero, J.M., et al. 2010, *Magnetic loops in the Quiet Sun*, ApJ 723, L185, [25 c, 3 c/y].
Wiegelmann, T., Thalmann, J.K., and Solanki, S.K. 2014, *The magnetic field in the solar atmosphere*, Astron.Astrophys.Rev. 22, 78, [39 c, 11 c/y].
Wiegelmann, T., Petrie, G.J.D., and Riley, P. 2017, *Coronal magnetic field models*, SSRv 210, 249, [8 c, 16 cy].

(6.5) Quiet Sun: Photosphere-Corona Connectivity

Abbett, W.P. 2007, *The magnetic connection between the convective zone and corona in the Quiet Sun*, ApJ 665, 1469, [102 c, 10 c/y].
Benevolenskaya, E.E., Kosovichev, A.G., Lemen, J.R., et al. 2002, *Large-scale solar coronal structures in soft X-rays and their relationship to the magnetic flux*, ApJ 571, 181, [34 c, 2 c/y].
Handy, B.H. and Schrijver, C.J. 2001, *On the evolution of the solar photospheric and coronal magnetic field*, ApJ 547, 1100, [21 c, 1 c/y].
Jendersie, S. and Peter, H. 2006, *Link between the chromospheric network and magnetic structures of the corona*, A&A 460, 901, [17 c, 1 c/y].
Lagg, A., Bruce, L., Harvey, J., et al. 2017, *Measurements of photospheric and chromospheric magnetic fields*, SSRv 210, 37, [6 c, 6 c/y].
Martinez-Gonzalez, M.H., Manso Sainz, R., Sensio Ramos, A., et al. 2010, *Small magnetic loops connecting the Quiet surface and the outer atmosphere of the Sun*, ApJ 714, L94, [41 c, 5 c/y].
Pevtsov, A.A. and Acton, L.W. 2011, *Soft X-ray luminosity and photospheric magnetic field in Quiet Sun*, ApJ 554, 416, [34 c, 2 c/y].
Priest, E.R., Heyvaerts, J.F., and Title, A.M. 2002, *A flux-tube tectonics model for solar coronal heating driven by the magnetic carpet*, ApJ 576, 533, [152 c, 10 c/y].
Ryutova, M., Habbal, S., Woo, R., et al. 2001, *Photospheric network as the energy source for the Quiet-Sun corona*, SoPh 200, 213, [23 c, 1 c/y].
Schrijver, C.J. and Title, A.M. 2002, *The topology of a mixed-polarity potential field, and interferences for the heating of the Quiet solar corona*, SoPh 207, 223, [57 c, 4 c/y].
Schrijver, C.J. and Title, A.M. 2003, *The magnetic connection between the solar photosphere and the corona*, ApJ 597, L165, [104 c, 7 c/y].
Titov, V.S., Hornig, G., and Démoulin, P. 2002, *Theory of magnetic connectivity in the solar corona*, JGR 107, A8, CiteID 1164, [163 c, 11 c/y].
Titov, V.S. 2007, *Generalized squashing factors for covariant description of magnetic connectivity in the solar corona*, ApJ 660, 863, [76 c, 7 c/y].

Uritsky, V.M., Davila, J.M., Ofman, L. et al. 2013, *Stochastic coupling of solar photosphere and corona*, ApJ 769, 62, [19 c, 4 c/y].
Wedemeyer-Böhm, S., Lagg, A., and Nordlund, A. 2009, *Coupling from the photosphere to the chromosphere and the corona*, SSRv 144, 317, [48 c, 6 c/y].
Wiegelmann, T., Solanki, S.K., Borrero, J.M., et al. 2013, *Evolution of the fine structure of magnetic fields in the Quiet Sun: Observations from Sunrise/IMAX and Extrapolations*, SoPh 283, 253, [10 c, 2 c/y].

(6.6) Quiet Sun: Alfvénic Waves

Campos, L.M.B.C. and Mendes, P.M.V.M. 2000, *On the dissipation rates for Alfvén waves in the solar transition region*, SoPh 191, 257, [5 c, 0.3 c/y].
De Pontieu, B., Martens, P.C.H., and Hudson, H.S. 2001, *Chromospheric damping of Alfvén waves*, ApJ 558, 859, [116 c, 7 c/y].
Khodachenko, M.L., Arber, T.D., Rucker, H.O. 2004, *Collisional and viscous damping of MHD waves in partially ionized plasmas of the solar atmosphere*, 422, 1073, [82 c, 6 c/y].
Leake, J.E., Arber, T.D., and Khodachenko, M.L. 2005, *Collisional dissipation of Alfvén waves in a partially ionized solar chromosphere*, A&A 442, 1091, [63 c, 5 c/y].
Malara, F., De Franceschis, M.F., and Veltri, P. 2005, *Dissipation of Alfvén waves in complex 3-D coronal force-free structures*, A&A 443, 1033, [8 c, 0.7 c/y].
Malara, F., Veltri, P., and De Franceschis, M.F., 2007, *Alfvén wave dissipation and topological properties of 3-D coronal force-free magnetic fields*, A&A 467, 1275, [8 c, 0.8 c/y].
McIntosh, S.W., De Pontieu, B., Carlsson, M., et al. 2011, *Alfvénic waves with sufficient energy to power the Quiet solar corona and fast solar wind*, Nature 475, 477, [261 c, 40 c/y].
Morton, R.J., Verth, G., Jess, D.B., et al. 2012, *Observations of ubiquitous compressive waves in the Sun's chromosphere*, Nature Comm. 3, 1315, [60 c, 11 c/y].
Sakai, J.I., Minamizuka, R., Kawata, T., et al. 2001, *Nonlinear torsional and compressional waves in a magnetic flux tube with electric current near the Quiet solar photospheric network*, ApJ 550, 1075, [13 c, 1 c/y].
Sakurai T., Ichimoto, K, Raju, K.P., et al. 2002, *Spectroscopic observation of coronal waves*, SoPh 209, 265, [53 c, 3 c/y].
Song, P. and Vasyliunas, V.M. 2011, *Heating of the solar atmosphere by strong damping of Alfvén waves*, JGR 116, A9, CiteID A09104, [21 c, 3 c/y].
Srivastava, A.K., Shetye, J., Murawski, K., et al. 2017, *High-frequency torsional Alfvén waves as an energy source for coronal heating*, Nature Scientific Reports 7, 43147, [9 c, 9 c/y].
Tomczyk, S., McIntosh, S.W., Keil, S.L., et al. 2007, *Alfvén waves in the solar corona*, Science 317, 1192, [402 c, 38 c/y].
Tu, J. and Song, P. 2013, *A study of Alfvén wave propagation and heating the chromosphere*, ApJ 777, 53, [16 c, 9 c/y].

(6.7) Quiet Sun: Heating Mechanisms

Aschwanden, M.J., Nightingale, R.W., and Alexander, D. 2000, *Evidence for nonuniform heating of coronal loops inferred from multi-thread modeling of TRACE data*, ApJ 541, 1059, [234 c, 13 c/y].
Aschwanden, M.J., Winebarger, A., Tsiklauri, D., et al. 2007, *The coronal heating paradox*, ApJ 659, 1673, [75 c, 7 c/y].
Cirtain,J.W., Golub,L., Winebarger,A.R., et al. 2013, *Energy release in solar corona from spatially resolved magnetic braids*, Nature 493, 501, [118 c, 26 c/y].

DeMoortel, I. and Browning, P. 2015, *Recent advances in coronal heating*, Philosophical Transactions Royal Society A 373, 2042, p.20140269, [27 c, 11 c/y].
De Pontieu,B., McIntosh,S.W., Carlsson,M., et al. 2007, *Chromospheric Alfvénic waves strong enough to power the solar wind*, Science 318, 1574, [460 c, 44 c/y].
De Pontieu, B., McIntosh, S.W., Carlsson, M., et al. 2011, *The origins of hot plasma in the solar corona*, Science 331, 6013, [212 c, 33 c/y].
Hahn, M., and Savin, D.W. 2014, *Evidence for wave heating of the Quiet-Sun corona*, ApJ 795, 111, [15 c, 4 c/y].
Hannah, I.G., Hudson, H.S., Hurford, G.J., et al. 2010, *Constraining the hard X-ray properties of the Quiet Sun with new RHESSI observations*, ApJ 724, 487, [24 c, 3 c/y].
Klimchuk, J.A. 2015, *Key aspects of coronal heating*, Royal Society of London Philosophical Transactions Series A, 373, p.20140256, [44 c, 18 c/y].
McIntosh, S.W., De Pontieu, B., Carlsson, M., et al. 2011, *Alfvénic waves with sufficient energy to power the Quiet solar corona and fast solar wind*, Nature 475, 477, [261 c, 40 c/y].
Priest, E.R., Foley, C.R., Heyvaerts, J., et al. 2000, *A method to determine the heating mechanisms of the solar corona*, ApJ 539, 1002, [96 c, 5 c/y].
Priest, E.R., Heyvaerts, J.F., and Title, A.M. 2002, *A flux-tube tectonic model for solar coronal heating driven by the magnetic carpet*, ApJ 576, 533, [152 c, 10 c/y].
Serio, S., Peres, G., Vaiana, G.S., et al. 1981, *Closed coronal structures. II. - Generalized hydrostatic model*, ApJ 243, 288, [272 c, 7 c/y].
Srivastava, A.K., Shetye, J., Murawski, K., et al. 2017, *High-frequency torsional Alfvén waves as an energy source for coronal heating*, Nature Scientific Reports 7, 43147, [9 c, 9 c/y].
Tomczyk, S., McIntosh, S.W., Keil, S.L., et al. 2007, *Alfvén waves in the solar corona*, Science 317, 1192, [402 c, 38 c/y].
Warren, H.P. and Brooks, D.H. 2009, *The temperature and density structure of the solar corona. I. Observations of the Quiet Sun with the EIS/Hinode*, ApJ 700, 762, [37 c, 4 c/y].
Winebarger, A.R., Warren, H.P., and Mariska, J.T. 2003, *TRACE and SXT active region loop observations: Comparisons with static solutions of the hydrodynamic equations*, ApJ 587, 439, [111 c, 8 c/y].

(6.8) Quiet Sun: EUV Nanoflare Energetics

Aschwanden, M.J., Tarbell, T.D., Nightingale, R.W., et al. 2000, *Time variability of the "Quiet" Sun observed with TRACE. II. Physical parameters, temperature evolution and energetics of EUV Nanoflares*, ApJ 535, 1047, [214 c, 12 c/y].
Aschwanden, M.J., and Parnell, C. 2002, *Nanoflare statistics from first principles: Fractal geometry and temperature synthesis*, ApJ 572, 1048, [112 c, 7 c/y].
Benz, A.O. and Krucker, S. 2002, *Energy distribution of microevents in the Quiet solar corona*, ApJ 568, 413, [76 c, 5 c/y].
Berghmans, D., Clette, F., and Moses, D. et al. 1998, *Quiet Sun EUV transient brightenings and turbulence. A panoramic view by EIT on board SOHO*, A&A 336, 1039, [106 c, 5 c/y].
Berghmans, D. and and Clette, F. 1999, *Active region EUV transient brightenings - First results by EIT of SOHO JOP80*, SoPh 186, 207, [186 c, 10 c/y].
Brkovic, A., Solanki, S.K., and Rüedi, I. 2001, *Analysis of blinkers and EUV brightenings in the Quiet Sun observed with CDS*, A&A 373, 1056, [35 c, 2 c/y].
Crosby, N.B., Aschwanden, M.J., Dennis, B.R. 1993, *Frequency distributions and correlations of solar X-ray flare parameters*, SoPh 143, 275, [345 c, 14 c/y].
Harrison, R.A., Harra, L.K., Brkovic, A., et al. 2003, *A study of the unification of Quiet-Sun transient-event phenomena*, A&A 409, 755, [22 c, 2 c/y].
Krucker, S. and Benz, A.O. 1998, *Energy distribution of heating processes in the Quiet solar corona*, ApJ 501, L213, [192 c, 10 c/y].
Parker, E.N. 1988, *Nanoflares and the solar X-ray corona*, ApJ 330, 474, [1025 c, 35 c/y].

Parnell, C.E. and Jupp, P.E. 2000, *Statistical analysis of the energy distribution of nanoflares in the Quiet Sun*, ApJ 529, 554, [188 c, 11 c/y].
Shimizu, T. 1997, *Studies of transient brightenings (microflares) discovered in solar active regions*, PhD Thesis, Natl. Astron. Obs., Mitaka, Tokyo, Japan.
Winebarger, A.R., Emslie, A.G., Mariska, J.T. et al. 2002, *Energetics of explosive events observed with SUMER*, ApJ 565, 1298, [30 c, 2 c/y].

(6.9) Quiet Sun: Fluxtube Braiding

Berger, M.A. and Asgari-Targhi, M. 2009, *Self-organized braiding and the structure of coronal loops*, ApJ 705, 347, [34 c, 5 c/y].
Berger, M.A., Asgari-Targhi, M., and Deluca, E.E. 2015, *Self-organized braiding in solar coronal loops*, J. Plasma Phys. 81/4, 395810404, [34 c, 5 c/y].
Cirtain, J.W., Golub, L., Winebarger, A.R., et al. 2013, *Energy release in the solar corona from spatially resolved magnetic braids*, Nature 493, 501, [118 c, 26 c/y].
Gudiksen, B.V. and Nordlund, A. 2002, *Bulk heating and slender magnetic loops in the solar corona*, ApJ 572, L113, [106 c, 7 c/y].
Gudiksen, B.V. and Nordlund, A. 2005a, *An ab initio approach to the solar coronal heating problem*, ApJ 618, 1020, [173 c, 14 c/y].
Gudiksen, B.V. and Nordlund, A. 2005b, *An ab initio approach to the solar coronal loops*, ApJ 618, 1031, [90 c, 7 c/y].
Hansteen, V., Guerreiro, N., De Pontieu, B., et al. 2015, *Numerical simulations of coronal heating through footpoint braiding*, ApJ 811, 106, [28 c, 11 c/y].
Knizhnik, K.J., Uritsky, V.M., Klimchuk, J.A., et al. 2018, *Power-law statistics of driven reconnection in the magnetically closed corona*, ApJ 853, 82.
Morales, L., and Charbonneau, P. 2008, *Self-organized critical model of energy release in an idealized coronal loops*, ApJ 682, 654, [23 c, 2 c/y].
Pant, V., Datta, A., and Banerjee, D. 2015, *Flows and waves in braided solar coronal magnetic structures*, ApJ 801, L2, [1 c, 0.4 c/y].
Parker, E.N. 1972, *Topological dissipation and the small-scale fields in turbulent gases*, ApJ 174, 499, [635 c, 14 c/y].
Peter, H., Gudiksen, B.V., and Nordlund, A. 2004, *Coronal heating through braiding of magnetic field lines*, ApJ 617, L85, [78 c, 6 c/y].
Pontin, D.I., Wilmot-Smith, A.L., Hornig, G., et al. 2011, *Dynamics of braided coronal loops. II. Cascade to multiple small-scale reconnection events*, A&A 525, A57, [50 c, 8 c/y].
Pontin, D.I. and Hornig, G. 2015, *The structure of current layers and degree of field-line braiding in coronal loops*, ApJ 805, 47, [11 c, 4 c/y].
Pontin, D.I., Janvier, M., Tiwari, S.K., et al. 2017, *Observable signatures of energy release in braided coronal loops*, ApJ 837, 108, [3 c, 3 c/y].
Prior, C. and Yeates, A.R. 2016a, *Twisted versus braided magnetic flux ropes in coronal geometry. I. Construction and relaxation*, A&A 587, A125, [1 c, 0.7 c/y].
Prior, C. and Yeates, A.R. 2016b, *Twisted versus braided magnetic flux ropes in coronal geometry. II. Comparative behaviour*, A&A 591, A16, [3 c, 2 c/y].
Schrijver, C.J., Hagenaar, H.J., and Title, A.M. 1997, *On the patterns of the solar granulation and supergranulation*, ApJ 475, 328, [61 c, 3 c/y].
Schrijver, C.J. 2007, *Braiding-induced interchange reconnection of the magnetic field and the width of solar coronal loops*, ApJ 662, L119, [29 c, 3 c/y].
Thalmann, J.K., Tiwari, S.K., and Wiegelmann, T. 2014, *Force-free field modeling of twist and braiding-induced magnetic energy in an active region corona*, ApJ 780, 102, [15 c, 4 c/y].
Wilmot-Smith, A.L., Hornig, G., and Pontin, D.I. 2009a, *Magnetic braiding and quasi-separatrix layers*, ApJ 704, 1288, [33 c, 4 c/y].

Wilmot-Smith, A.L., Hornig, G., and Pontin, D.I. 2009b, *Magnetic braiding and parallel electric fields*, ApJ 696, 1339, [42 c, 5 c/y].
Wilmot-Smith, A.L., Pontin, D.I., and Hornig, G. 2010, *Dynamics of braided coronal loops. I. Onset of magnetic reconnection*, A&A 516, A5, [46 c, 6 c/y].
Wilmot-Smith, A.L., Pontin, D.I., Yeates, A.R., et al. 2011, *Heating of braided coronal loops*, A&A 536, A67, [22 c, 3 c/y].
Wilmot-Smith, A.L. 2015, *An overview of flux braiding experiments*, Phil.Trans. Royal Soc. A 373, 20140265, [10 c, 3 c/y].
Yeates, A.R., Bianchi, F., Welsch, B.T. et al. 2014, *The coronal energy input from magnetic braiding*, A&A 564, A131, [7 c, 2 c/y].

(6.10) Quiet Sun: Radio Emission

Avrett, E.H. and Loeser, R. 2008, *Models of the solar chromosphere and transition region from SUMER and HERTS observations: Formation of the EUV spectrum of hydrogen, carbon, and oxygen*, ApJS 175, 229, [152 c, 16 c/y].
Bastian, T.S., Chintzoglou, G., De Pontieu, B., et al. 2017, *A first comparison of millimeter continuum and Mg II ultraviolet line emission from the solar chromosphere*, ApJ 845, L19, [1 c, 2 c/y].
Carlsson, M. and Stein, R.F. 2002, *Dynamic hydrogen ionization*, ApJ 572, 626, [139 c, 9 c/y].
Fontenla, J.M., Balasubramaniam, K.S., and Harder J. 2007, *Semiempirical models of the solar atmosphere. II. The Quiet-Sun low chromosphere at moderate resolution*, ApJ 667, 1243, [64 c, 6 c/y].
Fontenla, J.M., Curdt, W., Haberreiter, M., et al. 2009, *Semiempirical models of the solar atmosphere. III. Set of non-LTE models for Far-Ultraviolet/EUV irradiance computation*, ApJ 707, 482, [111 c, 13 c/y].
Gopalswamy, N., Yashiro, S., Mäkelä, P., et al. 2012, *Behavior of solar cycles 23 and 24 revealed by microwave observations*, ApJ 750, L42, [47 c, 9 c/y].
Kim, S., Park, J.Y., and Kim, Y.H. 2017, *Solar cycle variation of microwave polar brightening and EUV coronal hole observed by Nobeyama Radioheliograph and SDO/AIA*, J. Korean Astron. Soc. 50/4, 125.
Loukitcheva, M., Solanki, S.K., Carlsson, M., et al. 2004, *Millimeter observations and chromospheric dynamics*, A&A 419, 747, [56 c, 4 c/y].
Loukitcheva, M., White, S.M., Solanki, S.K., et al. 2017a, *Millimeter radiation from a 3-D model of the solar atmosphere. II. Chromospheric magnetic field*, A&A 601, A43.]
Loukitcheva, M.A., Iwai, K., Solanki, S.K., et al. 2017b, *Solar ALMA observations: Constraining the chromosphere above sunspots*, ApJ 850, 35, [5 c, 5 c/y].
Saint-Hilaire, P., Hurford, G.J., Keating, G., et al. 2012, *Allen Telescope Array multi-frequency observations of the Sun*, SoPh 277, 431, [2 c, 0.4 c/y].
Selhorst, C.L., Silva, A.V.R., Costa, J.E.R. 2005, *What determines the radio polar brightening ?* A&A 440, 367, [5 c, 0.4 c/y].
Selhorst,C.L., Gimenez de Castro,C.G., Varela Saraiva,A.C., 2010, *How are the EUV and radio polar limb-brightenings correlated?*, A&A 509, A51, [7 c, 1 c/y].
Shibasaki, K., Alissandrakis, C.E., and Pohjolainen, S. 2011, *Radio emission of the Quiet Sun and active regions (Invited Review)*, SoPh 273, 309, [47 c, 7 c/y].
Shimojo, M., Iwai, K., Asai, A., et al. 2017a, *Variation of the solar microwave spectrum in the last half century*, ApJ 848, 62.
Shimojo, M., Bastian, T.S., Hales, A.S., et al. 2017b, *Observing the Sun with the Atacama Large Millimeter/ submillimeter Array (ALMA): High-resolution interferometric imaging*, SoPh 292, 87, [4 c, 4 c/y].
Wedemeyer, S., Bastian, T., Brajsa, R., et al. 2016, *Solar science with the Atacama Large Millimeter / Submillimeter array - A new view of our Sun*, SSRv 200, 1, [32 c, 22 c/y].

White, S.M., Iwai, K., Phillips, N.M., et al. 2017, *Observing the Sun with the Atacama large millimeter/ submillimeter array (ALMA)*: Fast-scan single-dish mapping, SoPh 292, 88, [7 c, 7 c/y].

Wooten, A. and Thompson, A.R. 2009, *The Atacama Large Millimeter/submillimeter Array*, IEEE Proc. 97, 1463, [125 c, 15 c/y].